Journal of Experimental Nanoscience,
Vol. 1, No. 2, June 2006, 177–209

Taylor & Francis
Taylor & Francis Group

Electrospinning carbon nanotube polymer composite nanofibers

LESLIE Y. YEO* and JAMES R. FRIEND

Micro/Nanophysics Research Laboratory, Department of Mechanical Engineering, Monash University, Clayton, Vic 3800, Australia

(*Received December 2005; in final form March 2006*)

The unique and exceptional physical properties of carbon nanotubes have inspired their use as a filler within a polymeric matrix to produce carbon nanotube polymer composites with enhanced mechanical, thermal and electrical properties. A powerful method of synthesising nanofibers comprising these polymer composites is electrospinning, which utilises an applied electric stress to draw out a thin nanometer-dimension fiber from the tip of a sharp conical meniscus. The focussing of the flow due to converging streamlines at the cone vertex then ensures alignment of the carbon nanotubes along the fiber axis, thus enabling the anisotropic properties of the nanotubes to be exploited. We consider the work that has been carried out to date on various aspects encompassing preprocessing, synthesis and characterisation of these electrospun polymer composite nanofibers as well as the governing mechanisms and associated properties of such fibers. Particular attention is also dedicated to the theoretical modelling of these fiber systems, in particular to the electrohydrodynamic modelling of electrospinning polymer jets.

Keywords: Electrospinning; Carbon nanotubes; Polymer composites; Nanofibers; Electrohydrodynamics

1. Introduction

A carbon nanotube (CNT) is a seamless hollow cylindrical structure with a diameter of 1–2 nanometers, comprising of a hexagonal network of carbon atoms, one or both ends of the nanotube being capped with a hemispherical fullerene molecule [1]. In general, CNTs take two forms, namely single-walled nanotubes (SWNTs) and multi-walled nanotubes (MWNTs). SWNTs are single cylindrical layers of this carbon atom network, as shown in figure 1a, whereas MWNTs consist of several layers in the form of concentric cylinders bounded by weak van der Waals forces, as shown in figure 1b.

Due to the covalent bonding between the carbon atoms arising from sp^2 hybridisation, similar to that of graphite, CNTs exhibit a high surface area to volume ratio and hence very high tensile strength (typically 100–600 GPa), elastic

*Corresponding author. Email: leslie.yeo@eng.monash.edu.au

Journal of Experimental Nanoscience
ISSN 1745–8080 print/ISSN 1745–8099 online © 2006 Taylor & Francis
http://www.tandf.co.uk/journals
DOI: 10.1080/17458080600670015

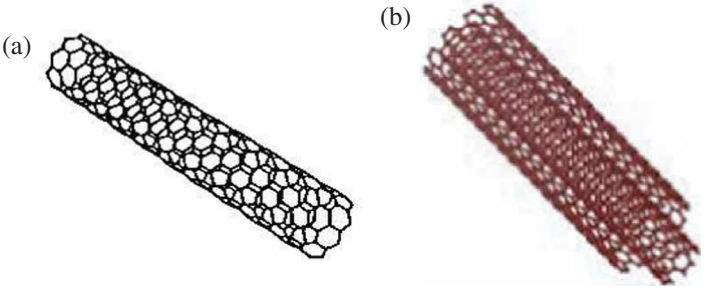

Figure 1. Schematic illustration of (a) a single-walled nanotube (SWNT), and (b) a multi-walled nanotube (MWNT).

modulus (typically 1–5 TPa) and compressive strength to weight ratios [2, 3]. They are extremely flexible due to their ability to reversibly absorb large stresses by deforming through twisting and buckling motions without fracturing [4, 5]. In addition, the structure of the molecular sites facilitates the possibility of tailoring its surface functionality to specific interfacial requirements for various applications [6].

The electrical and thermal properties of CNTs (SWNTs in particular since, unlike MWNTs, its atoms are bound in a single covalent network) are extremely anisotropic. The electrical conductivity depends on the chiral angle, which is the angle at which the atoms of the CNT are twisted about the main axis of the CNT. Bachilo *et al*. [7] classified these as 'armchair', 'zigzag' and 'intermediate' (or 'chiral') structures according to the chiral angle and diameter, as shown in figure 2. Armchair forms exhibit metallic properties and hence have extremely high conductivities and current densities whereas the zigzag and intermediate forms are either semi-conducting or semi-metallic. Both the thermal and electrical conductivities are observed to increase with alignment along the tube axis compared to the unaligned material [8]. These unique size, structural, and topological characteristics endow CNTs with excellent electromechanical, thermal, chemical and optical properties, demonstrating the potential of CNTs to revolutionise the development of nanocomposite materials and nanodevices [1, 9–11].

There are several methods currently used for the synthesis of CNTs. Among these are arc-discharge [1], laser ablation [12], vapour growth [13] and chemical vapour deposition [14]. These methods can produce aligned SWNTs and MWNTs but at low yields, and so remain prohibitively expensive. At present, no inexpensive high-yield production methods are known, though novel methods show promise, including fluidised bed reactors [15]. It should be noted that the vapour growth method produces vapour-grown carbon fibers (VGCF) which are similar in structure to MWNTs but with larger diameters, on the order of 100 nm.

CNTs tend to aggregate parallel to each other in tight bundles due to van der Waals forces [16], a problem in fabrication that prevents achievement of their superior physical properties, especially through exploitation of their inherent anisotropy. These bundles consist of a dense entangled network with a typical characteristic length scale of 10–100 nm and are prone to breakage when sheared at stresses significantly below that required to break a single nanotube along the CNT bundle axis [17–18]. Several techniques have therefore been developed to attempt orientation of individual

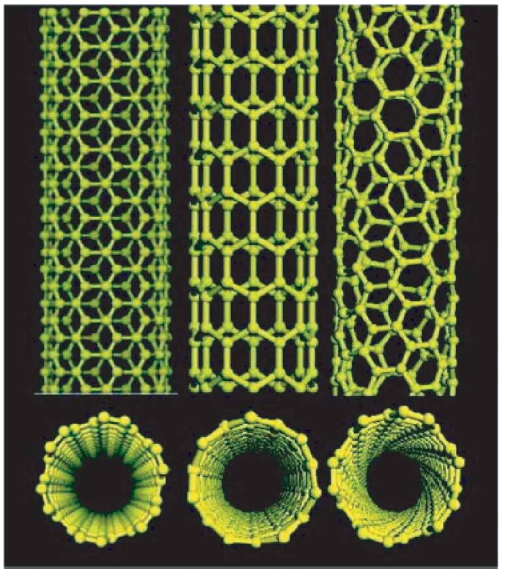

Figure 2. Schematic illustration of various carbon nanotube structural forms. (a) Armchair structure. (b) Zigzag structure. (c) Intermediate or chiral structure. Reproduced with permission from R.H. Baughman, A.A. Zhakidov, W.A. de Heer, *Science*, **297**, 787 (2002). Copyright (2002), American Association for the Advancement of Science.

CNTs along a single axis. In preparation for processing, CNT bundles are deagglomerated using ultrasonication [19] and ball-milling [20]. During solution processing, CNTs can also be aligned by directly introducing the aqueous CNT dispersion into a rotating poly(vinyl alcohol) solution, the induced shear resulting in CNT dispersion [21]. Other techniques that have been applied are the addition of surfactants to stabilise against aggregation [21], use of magnetic field alignment [22], spinning of extruded polymer composite melts [23], and, mechanical stretching [24, 25] and shearing [26, 27] of polymer/nanotube composite films. Schlittler *et al*. [28], on the other hand, considered the self-assembly of perfectly ordered carbon nanotube crystals deposited onto nanopatterned chemically modified substrates using thermolysis.

The other difficulty in exploiting the exceptional properties offered by CNTs for common applications is due to their very small sizes. Thus, methods are required to incorporate these nanoscale structures at the macroscopic level. One area in which active research is being pursued is the embedding of CNTs within a polymer matrix such that conventional polymeric fibers are reinforced to produce an ultra-light composite material with enhanced physical properties [29]. These reinforced polymer nanocomposite fibers with micron and nanometer diameters are extremely versatile materials which have a wide variety of applications in catalysis [30], electronic, optical or optoelectronic devices e.g. photocells, LEDs, highly conducting nanowires, etc. [31–34], filtration [35], lightweight and breathable textile materials for protective military clothing [36, 37], smart materials for aerospace vehicles [38, 39], and, piezo/pyro/ferro-electric sensor and actuator technology [40, 41]. A wide variety of other

possible applications are compiled in Breuer and Sundararaj [29] and Huang *et al*. [42]. Specific polymeric properties such as biodegradability and biocompatibility [43] have also been exploited such that polymer fibers are currently being used in biopharmaceutical and biotechnological applications, e.g. biosensors, wound care therapy, drug delivery and encapsulation, medical prostheses, and bioscaffolds for tissue and orthopaedic engineering [44–47], although biodegradable polymer nanocomposite fibers have yet to be fully explored.

Polymer/CNT composites have been synthesized through a host of fabrication methods, although there remains no high-yield commercial process for fabricating such composites. Among these are melt-mixing techniques such as extrusion, internal mixing, injection moulding and blow moulding ([29] and references therein), combination of solvent casting and melt mixing [48], film and spin casting [49], *in-situ* polymerisation [50], shear mixing [51], matrix-assisted pulsed laser evaporation [52], chemical vapour deposition growth of CNTs and deposition onto the surface of carbon fibers [53]. A detailed discussion of the different processing techniques is given in [29]. These widely different techniques, nevertheless, unite in the quest to limit filler (CNT) dispersion to avoid stress concentration localisation, maximise filler alignment whilst maintaining structural integrity of individual CNTs, and increase interfacial bonding between the filler and polymer matrix to enhance load transfer across the interface. In the absence of these requirements, the polymer/CNT composite is ineffective and the enhancement of its properties compromised.

A very powerful synthesis technique for fabricating polymer/CNT composite fibers is electrospinning. Of late, there has been an explosive growth in the use of electrospinning for fiber synthesis, and more recently, for the production of polymer nanocomposite fibers. Electrospinning provides a safe, low-cost and rapid one-step integrated processing assembly to produce continuous nanofibers, an advantage over other multi-step traditional discontinuous fiber template manufacturing methods. In addition, the technique can also be massively parallelised for mass fiber production without significantly affecting production costs. A comparison between nanofibers produced by electrospinning and other traditional fiber processing methods is shown in figure 3. Figure 3a compares the size of a typical carbon fiber produced commercially with that obtained by electrospinning whereas a comparison between figures 3b and c shows superior uniformity and sample purity of electrospun fibers over commercial vapour-grown fibers. Despite much work in the area, especially in the past decade, electrospinning is not well understood given the extremely complex electrohydrodynamic interactions that take place. In what follows, we will present a systematic overview of the developments in the electrospinning of polymer/CNT composite nanofibers.

It is not our intention to reproduce the comprehensive reviews in this area by Breuer and Sundararaj [29] and Huang *et al*. [42]. In Breuer and Sundararaj [29], the emphasis is on applications, processing methods (not restricted to electrospinning) and the physical properties of polymer nanocomposites. Huang *et al*. [42], on the other hand, limits their scope to electrospinning of polymer nanocomposite fibers, but focus is placed on applications, processing and characterisation methods. For completeness, we will present a concise overview of these topics; however, the emphasis here is to present a more in-depth treatment on electrospinning dynamics in relation to the

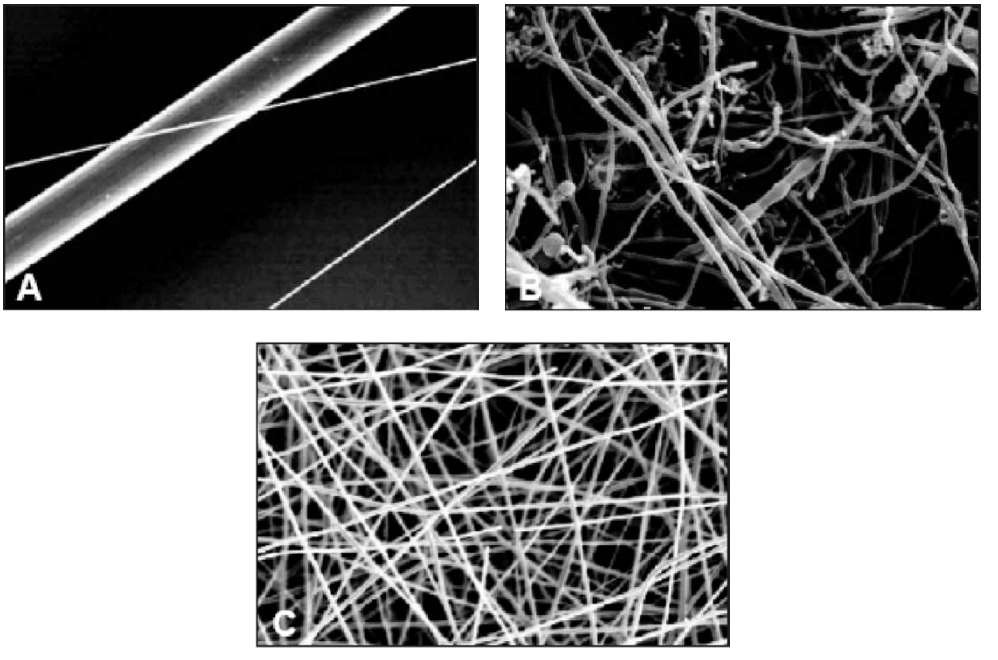

Figure 3. Comparison of nanofibers produced by electrospinning and other fiber processing methods. (a) The large fiber is a typical micron sized carbon fiber produced commercially whereas the small nanofibers are that produced by electrospinning. (b) Vapour grown commercial carbon fibers showing irregularities in size and homogeneity. (c) Electrospun carbon fibers which have superior uniformity. Reproduced with permission from Y. Dzenis, *Science*, **304**, 1917 (2004). Copyright (2004), American Association for the Advancement of Science.

production of polymer and polymer composite nanofibers. We note that the modelling nanofiber composites is very much in its infancy, given that it introduces a further degree of complexity to conventional fiber electrospinning. Nevertheless, we recognise that progress in this area is hampered by limitations in current understanding of the general electrospinning process. Particular attention will therefore be devoted to a systematic treatise examining theoretical models available for electrospinning and associated phenomena with the intention that a fundamental understanding of pure polymer electrospinning dynamics will lead to as well as encourage further work in the electrospinning of polymer composites.

In section 2, we provide an overview of the basic concepts and mechanisms of electrospinning for the production of micron and nanometer-sized fibers. The effects of system physicochemical parameters on fiber characteristics will be examined. In section 3, we proceed to discuss the developments in embedding carbon nanotubes in the fibers synthesised via electrospinning to form polymer nanocomposites. The theories for electrospinning of both polymer and polymer composite systems will then be reviewed in section 4. Finally, we will conclude with a brief discussion of future challenges.

2. Electrospinning

2.1. *Concepts and mechanism*

Electrospinning employs an electric field applied across a capillary and a ground electrode to draw out a jet of polymer solution from the capillary orifice, as illustrated in figure 4. Electrospinning has its origins in the electrospraying (otherwise known as electrohydrodynamic atomisation) process first observed by Zeleny [54], in which electrostatic charging is utilised to generate a spray of liquid aerosol drops issuing from the capillary tip of the liquid meniscus. Given that a wide range of monodispersed and polydispersed drop sizes can be produced down to several nanometers, electrospraying has been extensively investigated for applications including emulsification, agricultural and spray painting and fuel atomisation. More recently, electrospraying has emerged as a powerful soft ionisation technique for the generation of gas phase ions of large, complex and non-volatile biomolecules (e.g. DNA, peptides and proteins) in mass spectrometry [55]. As a result, the use of electrospraying is now widespread in genomic, proteomic and drug discovery research.

The first paper to appear on the electrospinning of polymer solutions was by Baumgarten [56], although several patents on fiber electrospinning were filed earlier, the first among many others by Fromhals [57] and Gladding [58]. In [56], fibers were drawn from the tip of a meniscus of acrylic solution emanating from the orifice of a capillary tube by means of an applied potential. The fibers were then collected on a grounded plate (figure 4). To maintain the size of the meniscus, an infusion pump was used to feed additional acrylic solution (acrylonitrile, methyl acrylate and sodium styrene sulfonate in dimethylformamide) through the capillary. In the past decade, there has been an exponential growth in interest in fiber electrospinning, yet the concept and technique have not evolved much beyond the original setup. Nevertheless, the technique has been used to produce a wide variety of polymeric fibers: polyethylene [59], poly(ethylene oxide) [60], polybenzimidazole [61] and polyethylene tetraphthalate/polyethylene naphthalate blends [62] are but a few examples. As interest in biomaterials for use as implantable devices has increased, a whole host of biodegradable polymers have also been electrospun. For example, Buchko *et al*. [63] produced a novel biocompatible film by electrospinning a silk-like protein polymer with fibronectin surface biofunctionality

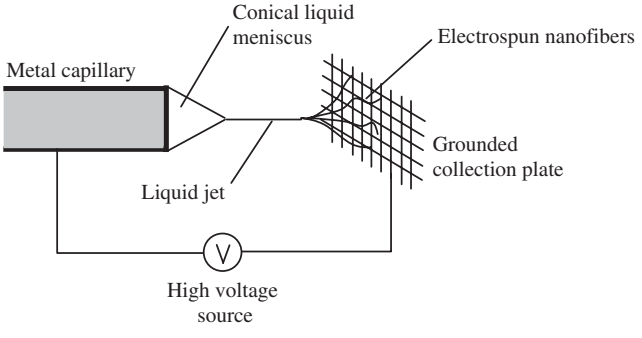

Figure 4. Schematic illustration of the electrospinning setup.

onto a substrate to be used as an implant, while Matthews *et al*. [64] and Kenawy *et al*. [65] produced collagen and poly(ethylene-co-vinyl alcohol) fibers, respectively, as bioscaffold supports for cell culturing and tissue engineering. High frequency ($>10\,\text{kHz}$) AC electric fields [66] have also been used to produce poly(lactic acid) fibers [47]; the advantages of using AC fields over DC fields, in particular for consumer applications and drug delivery, are discussed therein.

The underlying mechanism that governs the initial stage of the electrospinning process in which the polymer jet is drawn out from the liquid (polymer and solvent) meniscus is conceptually simple. The liquid meniscus protruding from the capillary orifice in the shape of a spherical cap has a capillary stress of order γ/R, where γ is the surface tension of the liquid and R is the principal curvature of the meniscus, of the same order as the radial capillary dimension. This capillary stress acts to restore any interfacial deformation. This is typically large since $R \sim 10^{-3}$–$10^{-4}\,\text{m}$. Thus, in order to pull out a thin jet from the tip of the meniscus, an externally-imposed stress must be applied to overcome the capillary stress. In the case of electrospinning, the electrical or Maxwell stress is given by $\varepsilon V^2/d^2$, where ε is the permittivity, V the applied voltage and d the electrode separation. Thus, balancing capillary and Maxwell stresses, it is possible to obtain an estimate of the critical voltage V_c which must be exceeded before a jet can emanate from the meniscus tip:

$$V_c \sim \sqrt{\frac{\gamma d^2}{\varepsilon R}}\,. \tag{1}$$

For typical conditions, $\gamma \sim 10^{-2}\,\text{kg/s}^2$, $d \sim 10^{-2}\,\text{m}$, $\varepsilon \sim 10^{-10}\,\text{C}^2/(\text{Jm})$ and $R \sim 10^{-4}\,\text{m}$, thus suggesting that extremely large voltages on the order of 10 kV are required to form a jet from the meniscus.

The jet ejection mechanism from the meniscus tip is a result of charge accumulation at the tip. If DC electric fields are employed, the charge separation time scale ε/κ, typically 10^{-5}–$10^{-7}\,\text{s}$, depending on the liquid conductivity κ, is much smaller than the hydrodynamic time scale L/U, where L and U are the characteristic axial length and velocity scales in the liquid meniscus; if $L \sim R$ for an unstretched meniscus, the latter is of order 10^{-3}–$10^{-4}\,\text{s}$. Thus, there is sufficient time for the formation of electric double layers at the meniscus interface. Due to tangential conduction, counter-ions then migrate towards the meniscus tip. At the tip, these like charges repel each other and result in Coulombic fission, resulting in the ejection of the jet; the critical conditions required for Coulombic fission are roughly given by equation (1). As a consequence of Coulombic fission, the resulting jet is charged. As the charged jet elongates under the action of the electric field, the large surface area to volume ratio of the jet, due to its small diameter ($\sim$100 nm–1 μm) results in evaporation of the solvent in which the polymer is dissolved, thus leaving behind a solidified polymer fiber. We note that the charge separation and subsequent tangential conduction in the liquid meniscus causes a tangential interfacial drag along the interface that leads to focussing of the meniscus into a sharp conical shape, as shown in figure 5. This phenomenon, known as the Taylor cone, will be discussed in section 4.1.

In flight, the jet/fiber is subject to Rayleigh (capillary), axisymmetric/azimuthal (varicose), whipping/bending, and other forms of instabilities. It has been suggested

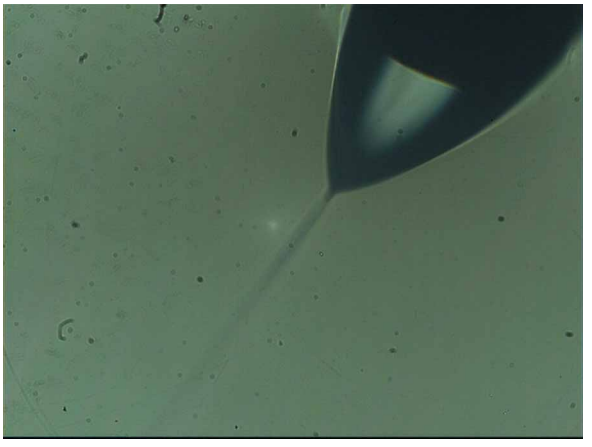

Figure 5. DC electrospraying/electrospinning meniscus showing the formation of a sharp Taylor cone from which a liquid jet emanates.

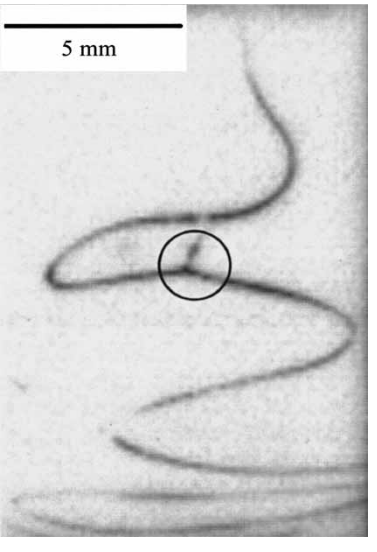

Figure 6. Whipping/bending instability of an electrospinning jet showing the spiral-like jet trajectory. The circle shows a section of the jet which splits to form a secondary jet, a process known as *splaying*. Reproduced with permission from D.H. Reneker, A.L. Yarin, H. Fong, S. Koombhongse, *J. Appl. Phys.*, **87**, 4531 (2000). Copyright (2000) American Institute of Physics.

that the bending instability controls fiber elongation and thinning, the other instabilities being predominantly responsible for pinching and hence drop formation [30]. At some distance from the tip, the straight jet/fiber undergoes a seemingly random coiling, bending, winding, spiraling and looping motion, the radius of the spiral-like trajectory and the fiber diameter increasing and decreasing, respectively, in a given cycle, as shown in figure 6 [67]. It was observed that these cycles are repetitive and appear to behave

in a self-similar fashion. Fiber alignment can be controlled to a certain extent by either suppressing the instability or by directing the electric field [68]. Suppression of the bending instability can be achieved by placing several ring electrodes around the jet such that multiple fields are introduced [69] or reducing the spinning distance [70]. On the other hand, Theron *et al.* [71] have designed a rotating ground electrode to direct the field such that the fiber can be continuously wound. This design involves sharpening the side edge of the grounded rotating collector, which provides a high field intensity toward which is depicted in figure 7.

Another instability that was observed was the bifurcation of the jet/fiber into two jets, known as jet splaying, the secondary jet trajectory being almost perpendicular to that of the primary jet, as shown in the circled section of figure 6 [67], although this was not seen universally [42, 59]. Other instabilities (e.g. kink and varicose instabilities) and spray modes have been observed in electrospraying when the applied voltage and flow rate is altered; these instabilities and modes are discussed in detail in the reviews by Clopeau and Prunet-Foch [72, 73] and Grace and Marijnissen [74]. While the spray modes are not as distinct in electrospinning, nevertheless some of the same instabilities are common to both electrospraying and electrospinning, and may manifest in beading along the fiber axis [75]; the beading phenomenon will be discussed further in the following section.

Although the formation of the liquid jet at the tip of the Taylor cone is mainly attributed to Coulombic instability, it is highly likely that viscoelasticity also plays a significant role in the jet elongation dynamics. This is supported by the existence of a threshold viscosity (and hence polymer concentration) required for the generation of fibers. Below this threshold value, solidified drops are produced [47]. The effect of solution viscosity will be discussed in the next section. The appearance of beading in the fiber morphology [75] also hints at the role of viscoelasticity. It is well known that axisymmetric/azimuthal instabilities in Newtonian jets lead to axisymmetric pinching to form satellite drops, as mentioned above. However, in non-Newtonian jets, filament beads are formed instead at the pinch points [76].

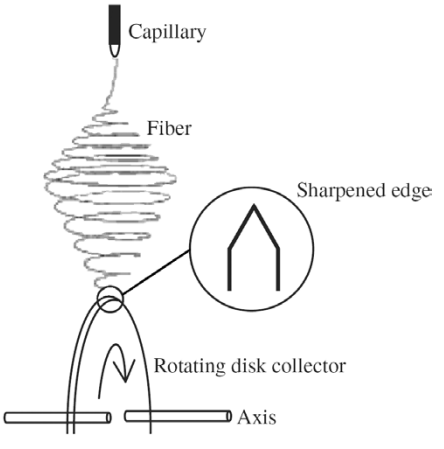

Figure 7. Schematic depiction of a rotating disk collector with sharpened edge used to collect the electrospun fibers. After Theron *et al.* [71].

Multiple fiber jets can also be produced. This multiple jet electrospinning mode is analogous to the multijet mode in electrospraying [73] and is an important consideration for the rapid mass production of fibers. In addition, a novel method for multiple jet electrospinning was proposed by Yarin and Zussman [77] in which an electric field is applied across a layer of polymer solution sitting above a ferromagnetic suspension layer, subjected to a normal magnetic field such that vertical spikes of the magnetic liquid invaded the polymer solution. The electric field then resulted in the instability of the bilayer interface giving rise to upward jets issued at the spike locations.

2.2. *Fiber characteristics*

The diameter of electrospun polymeric fibers are typically between 50 nm and 10 microns. Despite reports of the production of 3–5 nm fibers [78, 79], there are difficulties in reliably and uniformly producing fibers less than 50 nm for various materials [68]. There is also little agreement between data on the dependency of the fiber thickness on various system parameters. Whilst [59] report an inverse relationship between fiber diameter and the electric field (or applied voltage for a given constant electrode separation), Demir *et al*. [80] curiously show an increase in diameter with the applied voltage. Fong and Reneker [81] suggest that little variation in the diameter was observed when the electric field strength or solution viscosity (and hence polymer concentration) was altered, although they note that addition of salt to the solution led to a reduction in the fiber thickness. Nevertheless, others have reported increases in the fiber diameter with increasing viscosity or polymer concentrations [56, 75, 80]. In fact, there is a threshold viscosity (and hence polymer concentration), typically 10^3 cp, required for the generation of fibers, below which solidified drops are produced [47], as discussed in section 2.1. Nevertheless, a crucial issue on these measurements that perhaps explains the discrepancy in the trends is that the fiber diameter is not always constant, and hence a mean value would depend on the sample population of the measurements. Another source of discrepancy can be introduced by the ambient temperature, since the solution viscosity is highly sensitive to temperature [80]. Moreover, the fiber diameter will also depend on the bending instability discussed in section 2.1. In addition, Huang *et al*. [42] also noted that jet splaying (bifurcation) will affect the diameter of the fiber.

Deitzel *et al*. [75] have reported that the fiber morphology is strongly dependent on the various physicochemical parameters (solution viscosity, surface tension, concentration and dielectric permittivity) and the electric field. Changes in these parameters are suggested to give rise to different spray modes or instabilities, as discussed in section 2.1 and hence different final fiber morphologies. In other words, the final shape and form of the fibers are sensitive to the initial conditions and even the shape of the initiating drop to some extent, as shown in figure 8. Deitzel *et al*. [75] suggest that since step-discontinuities in the electrical current as the applied voltage is increased, usually associated with changes in the electrospray modes [82], are not observed in electrospinning, beading, as depicted in figure 9, is attributed to a result of the onset of instabilities at the meniscus from which the fiber/jet emanates rather than due to a change in the spray modes. They therefore suggest current control as a way to

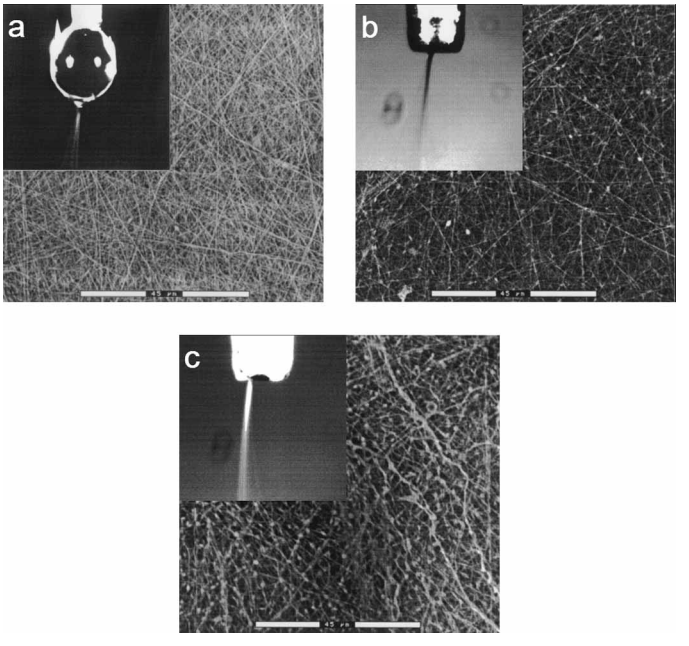

Figure 8. Effect of increasing the applied voltage on the electrospinning jet that emanates from the liquid meniscus and the resulting nanofiber morphology. The inset shows the jet from which the resulting fiber mesh is obtained. (a) 5.5 kV. (b) 7.0 kV. (c) 9.0 kV. Reproduced with permission from J.M. Deitzel, J. Kleinmeyer, J.K. Hirvonen, N.C. Beck Tan, *Polymer*, **42**, 261 (2001). Copyright (2001) Elsevier.

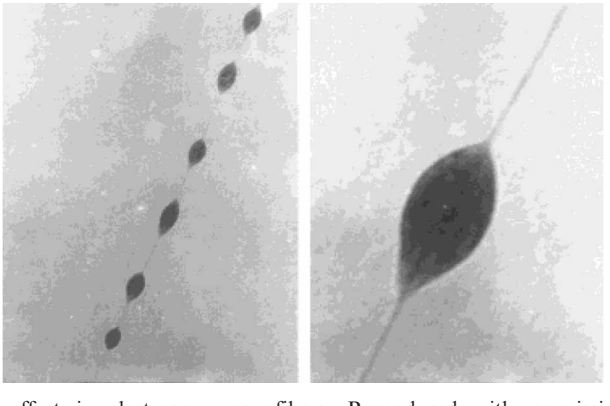

Figure 9. Beading effect in electrospun nanofibers. Reproduced with permission from H. Fong, D.H. Reneker, *J. Polym. Sci. B: Polym. Phys.*, **37**, 3488 (1999). Copyright (1999) Wiley Interscience.

reduce bead defects because the onset of beading can be observed when there is a change in the solution conductance. As discussed in section 2.1, viscoelastic effects could also lead to bead formation [76], although the effect of viscoelasticity in this context of bead formation in electrospinning jets has yet to be confirmed.

The solution concentration or viscosity also plays an important role in the fiber morphology. Increasing the polymer concentration is observed to regularise the cylindrical uniformity of the fibers; at low concentration, Deitzel *et al*. [75] observed the fibers to be irregular and undulating. Fong and Reneker [79] observed a reduction in beading density with higher concentrations. There is however an upper limit since the increase in the concentration and hence viscosity beyond a certain limit results in an instability at the tip as a result of the increasing difficulty of the syringe pump in providing constant flow through the orifice. Moreover, despite the reduction in the bead density, the beading does not completely disappear at high polymer concentrations, and beads were found to be larger in diameter and spindle shaped as compared to the smaller, more spherical beads, at low concentrations [42].

Surface tension was also found to affect bead formation, the lower the surface tension the lower the bead density [60]. Nevertheless, given the difficulty in varying surface tension independently of other parameters, it seems likely that this is a manifestation of the solvent composition [42]. The addition of salt, which results in an increased charge density and hence Maxwell stresses, has already been discussed above to lead to smaller fiber diameters. This increase in the uniaxial stretching force also leads to suppression of beading [44]. Nevertheless, it should be noted that increasing the electric field alone is not sufficient to decrease the occurrence of beading, as discussed above with reference to the work in [75]. It is an increase in the axial field in the direction of the fiber elongation that is required for more uniform fiber diameters. This is also consistent if viscoelasticity plays an important role in bead formation [76].

Another observed effect is nanopore formation on the fiber surface, as shown in figure 10 [83]. This effect is to be distinguished from the porosity measurements of fiber mesh networks used as bioscaffolds for tissue/orthopaedic engineering and for wound care therapy, a measure of the average interstitial space between neighbouring fibers in a network, determined using a mercury porosimeter [84]. The nanopores appear elliptical with their main axis oriented along the fiber axis and a longitudinal pore diameter typically 1/3 of the fiber diameter; the equatorial pore diameter is roughly 1/8–1/10 of the fiber diameter. Kim *et al*. [6] and Bognitzki *et al*. [83] attribute nanopore

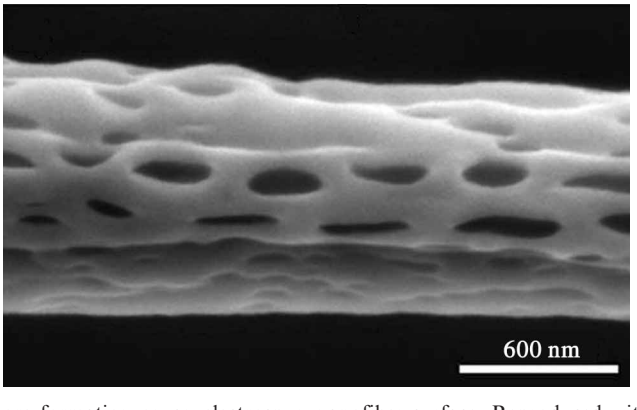

Figure 10. Nanopore formation on an electrospun nanofiber surface. Reproduced with permission from G.-M. Kim, G.H. Michler, P. Pötschke, *Polymer*, **46**, 7346 (2005). Copyright (2005) Elsevier.

formation to a thermodynamic instability during the electrospinning process in which phase separation via spinodal decomposition takes place as a result of rapid quenching (lowering of temperature) as the solvent evaporates from the emanating jet. The phase separation yields both solvent-rich and polymer-rich regions, the latter solidifying more quickly than the former; the pores are therefore a consequence of the solvent-rich regions. Few studies, however, have been carried out to quantify this as a function of the various system parameters. Nevertheless, this unique morphology creates the potential for increasing surface area, anchor sites for polymer matrix chain reinforcement and molecular binding sites for tailoring surface functionality in order to achieve a desired specificity [6].

Continuous coated polymer fibers, also known as core-shell (polymer-polymer and polymer-metal salt) fibers, have been produced through a co-axial electrospinning technique [85] in which two polymeric solutions or a combination of polymer solution and melt are extruded from concentric annular nozzles due to electric stresses, as shown in figure 11 [86]. Sun *et al.* [86] were able to produce poly(ethylene oxide)/poly(ethylene oxide) core-shell fibers, with different bromophenole (solvent) concentrations, and poly(ethylene oxide) shell fibers with cores comprising of poly(dodecylthiophene) or $Pd(OAc)_2$. Core diameters of approximately 200 nm and total fiber diameters of approximately 1 μm were obtained. Sun *et al.* [86] noted that poly(dodecylthiophene) does not form fibers alone by electrospinning due to its low molecular weight and attribute this to the role of poly(ethylene oxide) in the formation of a shell and template for the formation of poly(dodecylthiophene) fibers. On the other hand, the poly(ethylene oxide)/$Pd(OAc)_2$ fibers were metallicised by annealing the fibers such that $Pd(OAc)_2$ was converted to Pd, resulting in an improved core-shell morphology with a total diameter of 500 nm and a core diameter of 60 nm. Li and Xia [87] were also able to fabricate hollow titania nanofibers from core/shell fibers

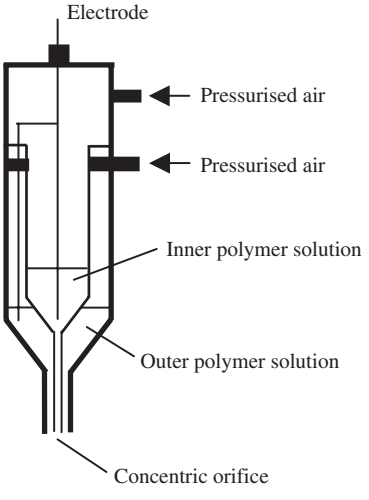

Figure 11. Co-axial electrospinning method for the production of continuous coated (core-shell) polymer fibers. After Sun *et al.* [86].

by selective removal of the poly (vinyl pyrrolidone) core through calcination of the fibers in air at high temperatures.

3. Synthesis of polymer nanocomposite fibers by electrospinning

The use of electrospinning to synthesise polymer/CNT nanocomposite fibers offers a possible way to simultaneously align CNTs along a single axis during processing without compromising the structural integrity of the individual CNTs. The focussing of the meniscus into a sharp conical shape gives rise to a converging flow and hence concentration of the streamlines in the extremely narrow region at the tip of the cone from which the jet and hence a fiber emanates, as shown in figure 5. As a result the CNTs dispersed in solution are oriented along the streamlines and hence along the fiber axis. The extremely large longitudinal strain rate of the emanating jet also ensues in the CNT alignment within the fiber. In contrast to agglomeration of embedded CNTs in the fiber, aligned CNTs within the fiber increases the effective contact area for interfacial bonding with the polymer matrix and enhances the effective aspect ratio for reinforcement [6]. We will discuss the possibility of alignment due to electric field induced dipole–dipole interactions in section 5.

For these reasons and because of the low cost and relatively uncomplicated process involved, electrospinning is quickly becoming an attractive and accepted technique for embedding CNTs within micron and nanometer sized polymeric fibers. A summary of the various polymer/CNT nanocomposite fibers generated by electrospinning is summarised in table 1. While it is not possible to provide a comprehensive list here, it suffices in demonstrating the viability and increasing popularity of using electrospinning to generate these polymer nanocomposites for various applications.

In order to obtain stable aqueous CNT dispersions, surfactants or amphiphilic polymers such as sodium dodecyl sulphate, poly(vinyl pyrrolidone) and natural polysaccharide Gum Arabic, which absorb onto the hydrophobic CNTs, are added [18]. The mixture is then sonicated for several hours after the addition of the dispersing agents thus creating a stable homogeneous dispersion. Subsequently, the dispersion is mixed with the polymer/solvent mixture and passed into a micro-syringe

Table 1. Summary of carbon nanotube polymer nanocomposites synthesized by electrospinning.

Polymer compound/solvent(s)	Filler	Filler concentration	Reference
Polycarbonate	MWNT	4 wt%	[6]
Poly(ethylene oxide)/Ethanol/Water/Sodium dodecyl sulphate	MWNT	3 wt%	[18]
Poly(ethylene oxide)/Ethanol/Water/Gum Arabic	MWNT	3 wt%	[18]
Polyimide/Dimethylformamide	SWNT	0.05 wt%	[38]
Polyacrylonitrile	SWNT	1–4 wt%	[88]
Polylactic acid	SWNT	1–5 wt%	[88]
Poly(vinylidene fluoride)/Dimethylformamide	SWNT	0–0.015 wt%	[89]
Polyacrylonitrile	SWNT	1 wt%	[90]
Polyacrylonitrile	MWNT	10 wt%	[91]
Polyamic acid/Acetic anhydride/Pyridine	SWNT	0.1–1 wt%	[92]
Poly(methyl methacrylate)/Nitromethane	SWNT	10 mg in 200 ml solvent	[93]

(typically several hundred microns in diameter) by means of a syringe pump. As with the electrospinning of conventional polymeric fibers, voltages of several kV (typically 10–30 kV) are applied across the syringe and the ground electrode, which consisted of a grounded disk rotating at several hundred rpm.

Nevertheless, CNT dispersion by sonication possibly introduces defects in the CNTs themselves [94]. Kearns and Shambaugh [94] suggest an optimum sonication period, below which inadequate dispersion is achieved and above which CNT damage or breakage resulted. Other means of CNT dispersion that could possibly circumvent this problem are the use of ball milling [20], AC electrophoresis [16, 95] and polymer wrapping [96] to overcome the van der Waals forces between the CNTs [16]. The latter employs reversible thermodynamic gradients such that the addition of polymer forms a tight association with the sides of the CNTs thereby disrupting the van der Waals interaction between CNTs and also the hydrophobic CNT interface with water [96].

The CNT surface can also be functionally modified to provide specificity for improved interactions between the CNT and its matrix, thus allowing the enhancement of processability and polymer composite properties, and permitting its coupling with other materials in its final integration into products [29, 97]. A summary of different approaches to chemical functionalisation is given in Breuer and Sundararaj [29], namely, covalent functionalisation, polymer/surfactant supramolecular adduct non-covalent exohedral functionalisation, chemical vapour deposition surface modification, plasma surface treatment and gamma radiation functionalisation.

Electrospun polymer nanocomposite fibers can be characterised through visual inspection of the CNTs, the polymer matrix and the CNT/polymer matrix interface in order to determine the CNT alignment in the fibers such that the fiber properties can be optimised. Dror *et al*. [18] examined electrospun polymer nanocomposite fibers with low electron dose transmission electron microscopy (TEM) with acceleration voltages of 120 kV by direct deposition of the fibers onto a perforated carbon-film-coated copper grid. In addition to TEM, Kim *et al*. [6] also utilised field emission gun-environmental scanning electron microscopy (FEG-ESEM). Nevertheless, optical and electron microscopy characterisation is not without its difficulties, in particular, due to the small length scales involved and hence the inability to distinguish between single CNTs [29]. Moreover, Breuer and Sundararaj [29] report difficulty in implementing electron microscopy due to issues with regard to sample preparation and the lack of polymer/CNT contrast. They list other methods, such as magnetic force microscopy (MFM) which exploits the interaction between the CNTs and the applied magnetic field, thus allowing direct visualisation of the polymer embedded CNTs [29] and scanning Kelvin microscopy which employs an oscillating probe to determine the conductivity distribution in heterogeneous materials such as the conducting CNTs in the insulating polymer matrix [98]. Yet another characterisation method that has been used is X-ray diffraction (XRD), as employed by Dror *et al*. [18]. In XRD, long exposure times, typically 1 day for wide-angle diffraction and 1–3 days for small-angle diffraction, are required due to the small CNT quantities [18].

Figure 12a and b show TEM images of MWCNT embedded electrospun poly(ethylene oxide) and polycarbonate fiber morphologies indicating some success of orienting individual CNTs along the fiber axis [6, 18]. Nevertheless, some degree

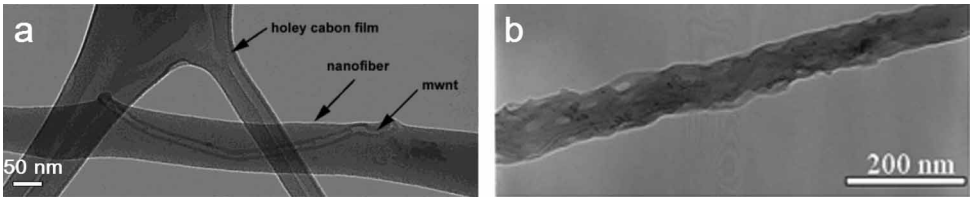

Figure 12. Transmission electron microscopy (TEM) images of carbon nanotube embedded polymer composite nanofibers showing alignment of the nanotubes along the fiber axis. (a) MWNT embedded poly(ethylene oxide) nanofiber. Reproduced with permission from Y. Dror, W. Salalha, R.L. Khalfin, Y. Cohen, A.L. Yarin, E. Zussman, *Langmuir*, **19**, 7012 (2003). Copyright (2003), American Chemical Society. (b) MWNT embedded polycarbonate nanofiber. Reproduced with permission from G.-M. Kim, G.H. Michler, P. Pötschke, *Polymer*, **46**, 7346 (2005). Copyright (2005), Elsevier.

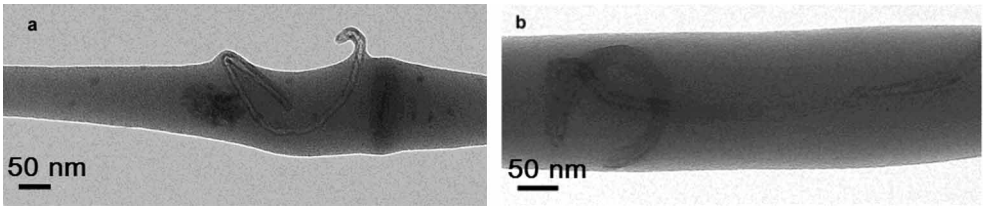

Figure 13. Transmission electron microscopy (TEM) images of carbon nanotube embedded polymer composite nanofibers showing irregularities in the alignment of the nanotubes within the fiber. (a) Protrusion of the nanotube from the fiber. (b) Entanglement of the nanotubes within the fiber. Reproduced with permission from Y. Dror, W. Salalha, R.L. Khalfin, Y. Cohen, A.L. Yarin, E. Zussman, *Langmuir*, **19**, 7012 (2003). Copyright (2003), American Chemical Society.

of convolution in the CNT orientation, entanglement and protrusion out from the fiber, which resulted in poor alignment of the CNTs along the fiber axis, were also observed, as shown in figure 13. Such irregularities were observed to be correlated closely with irregularities occurring in the fiber diameter. The source of the irregularities in the CNT orientation within the fiber is as yet unclear, although Dror *et al.* [18] offer two possibilities, i.e. the result of topological defects in the CNTs or the failure to completely stretch the CNTs as the fiber is ejected from the meniscus during the electrospinning process. By comparing cryo-TEM images of vitrified CNT dispersions with that of raw nanotubes, Dror *et al.* [18] suggest that irregularities could have possibly been introduced during the sonication process, consistent with the findings of Kearns and Shambaugh [94], which were reported above. Kim *et al.* [6] also suggest that the smaller the nanocomposite fiber diameter, the greater the tendency for curves to be introduced in the fiber. They attribute this to the curvature of the MWCNTs themselves, the thin fibers being unable to entirely accommodate or encapsulate these MWCNTs with large curvatures. In addition, they observe nanopore formation on the fiber surface to be suppressed due to insufficient space for phase separation to occur.

To study the *in situ* mechanical deformation of the electrospun nanocomposite fibers, Kim *et al.* [6] employed a novel method through the use of thermal stresses induced by a TEM electron beam. In this method, the impingement of the electron beam on the fiber results in local thermal expansion and hence tensile deformation,

the strain rate being controlled by the amount of beam flux applied [99]. This tensile strain results in fiber elongation and subsequent necking, the necking occurring specifically at the end of an embedded MWCNT. This is due to some slippage of the MWCNTs in the direction of the applied tensile stress occurring beyond a threshold stress value. Kim *et al*. [6] suggest that this CNT slip mechanism, coupled with the concentration of stress in the nanopore region (the nanopores form effective sites for which the stress concentration results in plastic deformation and hence necking) and the transfer of the mechanical load from the polymer matrix to the MWCNTs, is responsible for the enhancement of the critical fracture strain and also the increased toughness reinforcement of the fiber.

4. Electrospinning theories

4.1. *Taylor cone formation*

The formation of a sharp conical liquid meniscus in response to an applied electric field, as shown in figure 5, was first analysed by considering the relationship between the meniscus shape and the applied field [100]. This involved a static equilibrium dominant balance between the interfacial capillary and Maxwell stresses described by the normal stress jump across the meniscus interface. However, because the field on the surface is not known *a priori* and is strongly coupled to the interfacial shape, the solution of the problem is non trivial.

To decouple the hydrodynamics from the electric field, the analyses of Taylor [100] and other subsequent investigators [101, 102] assumed an *a priori* equilibrium conical shape, as depicted in figure 14. In the weak polarisation limit (negligible free space charge density), solution of the Laplace equation describing the electrostatics in the liquid and gas phases for the conical geometry in figure 14 in an axisymmetric spherical coordinate system $(r, \theta, 0)$ then gives the electrostatic potentials in the liquid and gas phases:

$$\varphi_l(r,\theta) = A_n r^n P_n[\cos\theta] \quad \text{for } \theta_0 \geq \theta \geq 0, \tag{2}$$

and

$$\varphi_g(r,\theta) = B_n r^n P_n[\cos(\pi-\theta)] = B_n r^n P_n[-\cos\theta], \quad \text{for } \pi \geq \theta \geq \theta_0, \tag{3}$$

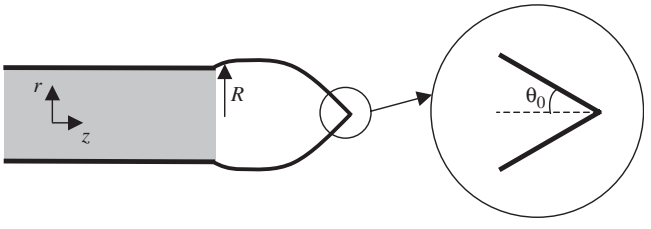

Figure 14. Schematic of electrospray/electrospinning meniscus with conical end.

r being the distance from the cone vertex of angle $2\theta_0$. In equations (2) and (3), $P_n[x]$ is the Legendre function of the first kind, and, A_n and B_n are constants. These equations together with the interfacial boundary conditions stipulated by continuity of potential and electric stresses across the interface then leads to [101, 102]

$$\varepsilon_g P_n[\cos\theta_0]P'_n[-\cos\theta_0] + \varepsilon_l P_n[-\cos\theta_0]P'_n[\cos\theta_0] = 0, \tag{4}$$

which has a solution $0 < n < 1$ for a given value of $\varepsilon_l/\varepsilon_g$ and θ_0; ε_l and ε_g are the relative permittivities of the liquid and gas phases, respectively. Since this results in an interfacial electric field E that scales as $1/r^{n-1}$, it then becomes clear from the normal stress jump across the interface

$$\Delta p = \gamma\kappa + \frac{\varepsilon_o(\varepsilon_l - \varepsilon_g)}{2}\left(\frac{\varepsilon_l}{\varepsilon_g}E_n^2 - E_t^2\right), \tag{5}$$

where Δp is the pressure difference across the gas–liquid interface, $\kappa = \cot\theta_0/r$ is twice the mean curvature of the interface, E_n and E_t are the normal and tangential components of the electric field, respectively, and, ε_o is the permittivity of free space, that solutions with $n = 1/2$ are to be admitted. Figure 15 depicts the solutions for the cone angle θ_0 as a function of the liquid to gas permittivity ratio, indicating that as $\varepsilon_l/\varepsilon_g \to \infty$, the exact solution of Taylor [100] for a perfectly conducting drop in which $\theta_0 \to 49.3^\circ$ is recovered. We note that two solution angles are possible for a given permittivity ratio; however, the larger of the two corresponds to an unstable equilibrium [101].

4.2. *Electrospinning model – Newtonian liquids*

The stability and dynamics of the electrospinning process has been studied through an analysis of electrically forced axisymmetric liquid jets [103]. Hohman *et al.* [103]

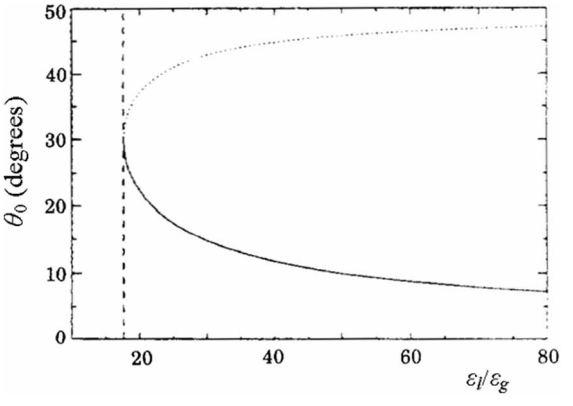

Figure 15. Cone angle θ_0 as a function of the liquid to gas permittivity ratio $\varepsilon_l/\varepsilon_g$. As $\varepsilon_l/\varepsilon_g \to \infty$, the exact solution of Taylor [100] for a perfectly conducting drop in which $\theta_0 \to 49.3^\circ$ is recovered. Reproduced with permission from H. Li, T.C. Halsey, A. Lobkovsky, *Europhys. Lett.*, **27**, 575 (1994). Copyright (1994), EDP Sciences.

adopted a *leaky dielectric* model [104] in which the asymptotic limit requirement of either assuming the liquid as a perfect conductor or a perfect dielectric in section 4.1 is relaxed such that the existence of free space charge at the interface q can be accounted for. This is because whilst bulk conduction can be neglected in the small free space charge density limit, interfacial charge and hence conduction is not usually negligible. The existence of such charge also gives rise to a finite tangential Maxwell stress which can only be balanced by the viscous stress.

The bulk gas and liquid phases are assumed to be electroneutral and hence the electric potential in each phase is described by the Laplace equation. This is supplemented by the boundary conditions that describe continuity of the electric potential and the tangential and normal components of the electric field across the interface. A far-field boundary condition is also imposed to account for the applied field. In addition, interfacial charge conservation applies:

$$\frac{\partial q}{\partial t} + \mathbf{u} \cdot \nabla q - q\mathbf{n} \cdot (\mathbf{n} \cdot \nabla)\mathbf{u} = \nabla^2 q + \sigma_l E_{n_l} - \sigma_g E_{n_g}, \tag{6}$$

where t is the time, $\mathbf{u} = (u, 0, w)$ is the velocity vector in the liquid for an axisymmetric cylindrical coordinate system $(r, 0, z)$ and σ denotes the conductivity; the subscripts l and g denote the liquid and gas phases, respectively, and $\mathbf{n}$ is the unit normal vector.

In the liquid phase, the usual hydrodynamic equations governing the conservation of mass and momentum apply together with the boundary conditions that describes the continuity of tangential stresses and the jump in the normal stresses across the interface. In addition, a kinematic boundary condition can also be prescribed at the interface to give an evolution equation for the jet radius $R(z, t)$. An important underlying assumption of the electrospinning model is that the jet is slender, i.e. the radial length scale R_o is much smaller than the axial length scale L, or $\delta \equiv R_o/L \ll 1$, such that the slender body theory or long wave approximation can be utilised. This allows the external electric field to be simplified such that a slender dielectric meniscus can be described as an effective axial line distribution of free and interfacially bound charges $\lambda(z)$ [105]. Applying an electric field flux balance on Gaussian surfaces surrounding the meniscus interface and substituting into Coulomb's Law, which describes the gas phase electric potential in the region far from the interface, then yields a second order ordinary differential equation for the tangential electric field in the liquid phase [103]:

$$E_{t_l} - \ln \delta \left[\frac{1}{2} \left(\frac{\varepsilon_l}{\varepsilon_g} - 1 \right) \left(R^2 E_{t_l} \right)_{zz} - 4\pi (qR)_z \right] - E_\infty = 0. \tag{7}$$

By scaling the governing equations above with the appropriate transformations for the slender body problem, it is possible to write down a set of coupled nonlinear partial differential equations that describe the spatio-temporal evolution of the interfacial height R, axial velocity w and interfacial charge density q, all of which involve the tangential liquid electric field, and hence are coupled to equation (7). We note that in this problem, the leading order terms in the long wave expansion is inadequate to describe the dynamics of the axisymmetric jet; higher order correction and, more specifically, the extensional stresses w_{zz} play an important role in the axisymmetric jet dynamics [106].

Boundary conditions are specified by the nozzle radius, appropriately scaled, for $R(z=0)$, and an asymptotic matching condition for the jet profile as $z \to \infty$ given by Kirichenko *et al.* [107]. Far from the nozzle, the dominant forces responsible for the stretching of the jet involves gravitational (for inclined capillaries), inertial and tangential Maxwell stresses. Balancing these forces then led to $R(z) \sim z^{-1/4}$, from which a jet profile can be derived [108]. The remaining conditions are the description of the far field, $E_t \to E_\infty$ discussed earlier and the interfacial charge density at the nozzle $q(z=0)$.

However, Hohman *et al.* [109] admits that the asymptotic equation for the external field in the slender body limit, i.e. equation (7), is impractical due to the difficulty in specifying physically meaningful boundary conditions, as stated above. In addition, equation (7) also breaks down near the nozzle. Instead, Hohman *et al.* [109] propose an asymptotic version of Coulomb's law using the Method of Images wherein image charges are imposed to account for the polarization of the jet. However, to recover the constant potential conditions at the nozzle surfaces $z=0$ and $z=d$, assumed to resemble parallel capacitor plates, an infinite number of image charges are required such that the construction of a Green's function for the electric potential requires an infinite summation of all the potential contributions of each image charge. As this becomes mathematically tedious, Hohman *et al.* [109] retain only the first terms, and hence the external electrostatic potential reads

$$\Phi_g \sim \Phi_\infty + \int_0^d dz' \lambda(z') \left[\frac{1}{\sqrt{R(z)^2 + (z-z')^2}} - \frac{1}{\sqrt{R(z)^2 + (z+z')^2}} - \frac{1}{\sqrt{R(z)^2 + (2d-z-z')^2}} \right], \tag{8}$$

where Φ_∞ is the far-field potential. Nevertheless, they assert that the introduction of the error associated with the truncation of successive terms is acceptable and sufficient for fixing the boundary conditions at the nozzle since the electric field solution accuracy increases in this vicinity. Equation (8) is then solved numerically together with the equations that govern the conservation of mass, momentum and interfacial charge to give steady-state solutions of the axisymmetric jet profile as a function of the flow rate and applied voltage.

Hohman *et al.* [109] report that their electrospinning experiments show the current to be an approximately linear function of the imposed flow rate and applied field, which differs from electrospraying where the current I is typically independent of voltage and scales as the square root of the flow rate. Theoretically, the current can be determined by the boundary conditions imposed, i.e.

$$I = \frac{\partial q}{\partial t} = 2\pi R(z=0) q(z=0) + \sigma_l \pi R(z=0)^2 E_t(z=0), \tag{9}$$

i.e. the current is equivalent to specifying the charge density at the nozzle, which in turn is fixed by the governing equation for charge transport along the capillary towards the nozzle [109]. Once the charge density at the nozzle is known, the current is fixed and the electric field at every position can be determined. The alternative procedure in [109], i.e. equation (8) used in conjunction with the hydrodynamic equations of motion and

the interfacial charge conservation equation given by equation (6), however, cannot specify the current and hence the interfacial charge density. This is a crucial factor for the stability of the jet, implying that the jet stability is sensitive to the upstream conditions at the nozzle (nozzle shape and electrode properties e.g. material and protrusion length), justified by the argument that this has been observed in previous experimental electrospray studies. The determination of the current, as stipulated by equation (9), therefore amounts to establishing a relationship between the interfacial charge density and the electric field at the nozzle, i.e. $q(z=0)$ and $E_t(z=0)$. However, this is non-trivial and involves both equations (6) and (8), i.e. the current is therefore globally dependent on the jet profile as well as the charge density and field along it. Hohman *et al.* [109] therefore opted for a refinement strategy by iterating between numerical solutions for various boundary conditions with a controlled set of experiments to determine an effective boundary condition.

Solutions at steady-state could however only be found when the charge density at the nozzle $q(z=0)$ was extremely small, in particular, when the normal field is negligible compared to the tangential field [109]. A ballooning effect was observed when the charge density at the nozzle is large due to co-ion repulsion, leading to jet destabilisation. This is clearly an artifact of the numerical model since an underlying assumption invoked in the derivation of the governing equations, in particular the slender body theory of equation (7), is that the radial charge relaxation time scale is much smaller than that for axial charge relaxation. This assumption breaks down close to the nozzle where the radial and length scales become comparable, i.e. the jet is no longer slender. In the absence of radial charge relaxation, there is hence no charge buildup at the interface. Nevertheless, even with liquids of higher conductivity, long wave instabilities still occur even in the limit $q(z=0)=0$, which is contradictory to experimental observations [108].

The ballooning problem, introduced by the boundary condition for $q(z=0)$ in [109] was resolved by Feng [108], Ganan-Calvo [110] and Hartman *et al.* [111]. Feng [108] raises the philosophical question of whether the origin $z=0$ is actually located on the jet itself and suggests that geometrical details and the applied external field are that which sets the boundary condition for $q(z=0)$. As such details are not accounted for by the numerical model, an alternative condition is required. Both Ganan-Calvo [110] and Hartman *et al.* [111] instead impose the slope of the jet R_z at the entry region $z=0$. Feng [108] also suggests that his results show that $q(z=0)$ is not a free parameter but rather is constrained physically by some condition not accounted for in the model. Therefore, he used the differential equation in equation (7) for the axial field instead of the integral potential equation in equation (8) used by Hohman *et al.* [109] and did not find any existence of jet ballooning. They suggest that the reason why this is so is because equation (8) requires the jet profile $R(z)$ to be continuous and to vanish at both the entry and exit [105]. Whilst this is obeyed at the exit where $q(z\to\infty)\to 0$ and $R(z\to\infty)\to 0$ and hence lacks an electric field, this is not true at the nozzle. In other words, equation (8) fails to account for the effect of charge upstream of the nozzle, and hence the philosophical requirement that the slender jet must originate prior to the nozzle orifice where a true jet is issued. The consequence of this failure is the underestimation of the tangential field along the jet, resulting in the jet ballooning effect due to radial charge repulsion. The use of equation (7), in contrast, avoids the need to

account for upstream charge effects or geometrical detailing of the nozzle such that the slender body approximation can be applied downstream of the nozzle. However, it does require either the specification of either $q(z=0)$ or $E_t(z=0)$ as a trade-off, as discussed above. Nevertheless, Feng [108] used several values for $q(z=0)$ but found the results outside a thin boundary layer near the nozzle insensitive to this boundary condition.

4.3. *Electrospinning model – non-Newtonian liquids*

The model above, in which a Newtonian liquid jet was assumed, was extended by Feng [108] to account for non-Newtonian behaviour. Unfortunately, electrospinning does not exhibit pure strain hardening (viscoelastic) behaviour in which elongation is commenced from rest such that the transient extensional viscosity increases rapidly with the strain but neither does it exhibit pure steady-state extension (viscous) such that the steady-state extensional viscosity increases (extensional thickening) or decreases (extensional thinning) with the strain. Viewed from a Lagrangian perspective, the fluid particle in electrospinning already possesses some strain history within the nozzle and subsequently is subject to uniaxial extensional stresses with a time-dependent strain rate [108]. Feng [108] nevertheless explored both pure viscoelastic and pure viscous cases in turn.

In the pure viscous case, the polymeric solution is assumed to experience universal steady stretching at a local strain rate, corresponding to the small Deborah number limit. The steady elongational viscosity $\bar{\mu}$ is then given by a universal viscosity for shear, extensional and mixed flows [112]:

$$\bar{\mu} = \mu_o \left[1 + \left(\lambda \sqrt{\frac{\dot{\Gamma}_{\mathrm{II}}}{2}} \right)^2 \right]^{n-1/2} \left[\mathrm{Tr}_\infty + (3 - \mathrm{Tr}_\infty)\left(1 + \omega^3 \left|\dot{\Gamma}_{\mathrm{III}}\right|\right)^{m-1/3} \right], \tag{10}$$

where μ_o is the Newtonian (zero strain rate) viscosity, $\dot{\Gamma}_{\mathrm{II}} = 6(dw/dz)^2$ and $\dot{\Gamma}_{\mathrm{III}} = 6(dw/dz)^3$ are the second and third variants of the strain rate tensor, λ and ω are the shear and extensional relaxation times, Tr_∞ the asymptotic Trouton ratio at high strain rate, and, n and m are the shear and extensional power law indices. In pure extensional thinning ($m=1$), Feng [108] observed the axial tensile force to resist stretching such that extensional thinning is found to promote stretching for slightly strained jets. In contrast, the axial tensile force was found to delay stretching in the case of high extensional thinning (small n values) for pure extensional thinning fluids. In particular, stretching is prevented near the nozzle but increases with axial distance. On the other hand, larger viscosities resist stretching for both slightly and severely strained jets for fluids which thicken at low strain rates and thin at high strain rates.

In the viscoelastic case, an empirical function was used to approximately account for memory effects [108]:

$$\frac{\bar{\mu}^+}{3\mu_o} = \begin{cases} \exp\left\{ p\left[1 - \cos\left(\pi \dfrac{\Gamma^2}{\Gamma_s^2} \right) \right] \right\} & \text{if } \Gamma \le \Gamma_s \\ \exp(2p) & \text{if } \Gamma > \Gamma_s \end{cases}, \tag{11}$$

where Γ is the Hencky strain and Γ_s the strain at which a steady-state extensional viscosity is achieved; p is a parameter that determines the steady-state Trouton ratio. The effect of equation (11) is to increase the axial gradient of the tensile stress. A further assumption is imposed in which the jet exits the nozzle at a prestrained rate Γ_0 and increases downstream along the jet by

$$\Gamma - \Gamma_0 = \int \dot{\Gamma}\, dt = \int \sqrt{3} w'\, dt = \int_0^z \sqrt{3} \frac{w'}{w}\, dz = \sqrt{3} \ln w. \tag{12}$$

Feng [108] observed the stretching to increase upstream but diminish downstream due to strain hardening, leading to larger fiber radiuses. An alternative formulation was also derived by Spivak *et al*. [113] in which the Oswald-deWaele nonlinear power law constitutive equation was employed to describe the rheological behaviour of the polymeric liquid.

4.4. *Electrospinning model – bending instabilities*

By performing a stability analysis on the governing equations in section 4.2, Hohman *et al*. [103] identified 3 different instabilities, namely the classical Rayleigh (capillary) hydrodynamic instability, and the azimuthal/varicose and the whipping/bending instabilities induced by the electric field on a liquid of finite conductivity. The jet is straight but its radius thins in the azimuthal/varicose instability whereas the radius is constant but the jet direction varies for the bending instability; the varicose instability is therefore the azimuthal counterpart of the classical Rayleigh capillary instability when electric field effects are dominant. Naturally, it is also observed that the varicose and bending instabilities, both of which are present only for conducting liquids, are enhanced with increasing electric field intensity whereas the classical Rayleigh capillary instability is suppressed. The dominance between the latter instabilities was also observed to be dependent on the jet radius and the interfacial charge density. The bending instability, in particular, is strong for highly conducting fluids. It tends to dominate when the interfacial charge density and the jet radius are both large, whereas the varicose instability dominates when the interfacial charge density and jet radius are low.

Hohman *et al*. [109] therefore suggest that it is the triggering of the bending instability due to the interaction of the interfacial charge with the electric field in highly conducting fluids resulting in the suppression of the varicose instability that gives rise to the onset of electrospinning. They present operating diagrams that show the competition between these two instabilities and therefore indicate the regime in which electrospinning is possible. Hohman *et al*. [109] also insist that their findings are consistent with the occurrence of a stable *cone jet* mode for electrospraying [72, 73], which is shown to be recovered in the limit of low viscosity and highly conducting (and hence high interfacial charge density) liquids where the varicose instability is suppressed, thus allowing for a stable liquid jet at lower critical flow rates. One further postulation made by Hohman *et al*. [109] is that the *splaying* phenomenon observed experimentally in which the primary jet splits into multiple jets is an optical illusion

of small lateral disturbances along the jet axis, which can be observed if higher resolution images with shorter exposure times are obtained.

Other important parameters which can influence the instability are the liquid viscosity and dielectric permittivity, the effect of viscosity being to decrease the wavelength where the bending instability is most likely to appear to low wave numbers, consistent with experiments where long wavelength instabilities are observed. However, viscosity is also seen to reverse the dominance between the varicose and bending instabilities, contradicting experimental results [103]. This is reconciled by recognising that the effect of viscosity cannot be assessed independently of the effect of the interfacial charge density, since the interfacial charge resists viscous stabilisation. Both viscosity and interfacial charge must therefore be taken into consideration. The observations above are also complicated by the fact that the interfacial charge density decays as the jet thins [109]. This is because mass conservation requires the jet velocity to increase as the jet radius shrinks. As $R \to 0$, the conduction current in equation (6) becomes negligible and advection dominates, thus 'stretching' the effective area of the interfacial charge and decreasing the interfacial charge density. For core-shell fibers generated by the co-axial electrospinning method, Sun *et al.* [84] suggest that since the characteristic time scale for the bending instability is large compared to the diffusion time scale for the various polymers in the heterogeneous solution and the time for the propagation of the polymer-polymer interface, the interface between the polymers are maintained despite the instability.

A different approach to modelling the bending instabilities was adopted by Reneker *et al.* [67] wherein a rectilinear viscoelastic jet segment in the presence of an electric field is represented by a dumbbell whose ends assume both finite mass m and charge e. One end is fixed and the other, connected by a spring with length l, is acted upon by the Coulombic repulsion force $-e^2/l^2$ and the force arising from the applied electric field $-eV/d$, thus pulling the two dumbbell ends apart; V is the applied voltage and d the separation. A restoring force, as represented by the spring between the two dumbbell ends, however acts to restrain their separation and is given by a phenomenological rheological model for concentrated polymeric suspensions under strong extensional stresses. An expression for the restoring force, dependent on viscosity, elastic modulus and filament length, as a function of time due to stress relaxation effects can then be solved numerically together with the conservation of mass and momentum of the dumbbell subject to appropriate initial conditions.

To model the bending instability, Reneker *et al.* [67] applied a time-dependent small bending displacement disturbance or perturbation, which is assumed to arise from the instability associated with a static system of charges in the absence of an external electric field, the so-called Earnshaw instability [114]. A linearised description of the growth rate of this perturbation is then shown to increase exponentially which is sustained due to the decrease in the electrostatic potential energy during the growth of the spatial perturbation. The bending action is then governed by the balance between this destabilising Coulombic effect and the stabilising viscoelastic and capillary effects.

A complete model of the electrospinning jet is then described by constructing an interconnected system of such viscoelastic dumbbells in series. To represent the flow, additional dumbbells are incrementally added to the fixed position at the origin where the physical orifice would be located. The Coulombic interaction between each end of

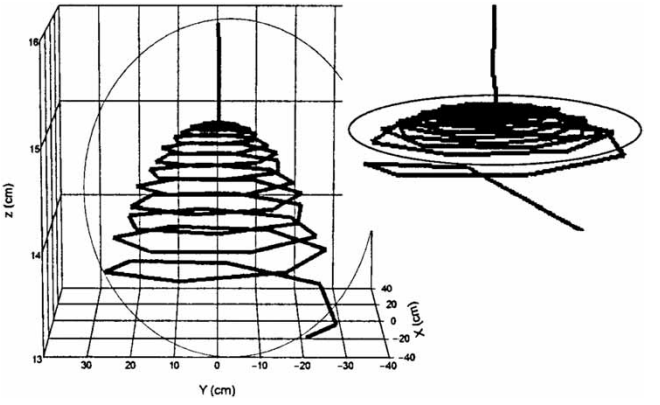

Figure 16. Simulation of whipping/bending instability arising in a non-Newtonian electrospinning liquid jet as a result of the transient growth of a small imposed spatial disturbance. Reproduced with permission from D.H. Reneker, A.L. Yarin, H. Fong, S. Koombhongse, *J. Appl. Phys.*, **87**, 4531 (2000). Copyright (2000), American Institute of Physics.

the dumbbell with all other ends therefore must be accounted for by summing over each individual interaction. The reader is referred to the complete derivation of the model in [67]. The trajectory of the jet can then be mapped by solving the governing equations for the system of viscoelastic dumbbells. In time, due to temporal growth of the Earnshaw instability, the dumbbell ends are observed to move progressively apart such that the trajectory resembled a helical fractal-like structure as shown in figure 16, in similar fashion to an electrospinning jet undergoing bending instabilities.

Yarin *et al.* [115], on the other hand, utilised the localised-induction approximation to determine the net Coulombic force acting on an element in a thin electrospinning jet that results in bending. This is based on a loose analogy between the bending instability found to occur in electrospinning jets with aerodynamic bending instabilities in which a distributed lift force acts on a jet as a result of the Bernoulli principle and is a principal source of the jet instability. This replaced the viscoelastic dumbbell model of Reneker *et al.* [67] in the calculation of the electric force. However, an approximate cut-off length for the force integral is required and had to be obtained externally by solving another model. Lagrangian non-Newtonian jet dynamics was modelled by deriving a set of continuous, quasi-one-dimensional nonlinear partial differential equations and solving the discretised versions to obtain the jet trajectory. In their model, shear forces and bending stiffness are neglected on the premise that the jet is thin. From this model, Yarin *et al.* [115] were also able to investigate the stability dynamics of small bending disturbances.

4.5. *Model for composite nanofibers*

As suggested in the introduction, few investigations have been carried out to model composite nanofibers. The little work that has been carried out in this area is mainly restricted to fiber composites themselves, produced via other fabrication techniques; a short section of this has been discussed in [42]. One particular issue raised by

Grigoras *et al*. [116] is whether continuum models are valid at the nanoscale. Others argue that modelling at the micro-scale, in particular, using micromechanics still warrants merit in describing overall mechanical properties of composite nanofibers such as the fiber elastic properties [42]. Nevertheless, we also anticipate the use of molecular dynamic simulations in the near future.

A theoretical model has been derived by Dror *et al*. [18] for electrospinning CNT embedded polymeric nanofibers. The basis for the model is a sink-like flow towards the vertex of a wedge, which represents the Taylor cone. In fact, Dror *et al*. [18] suggest that the converging streamlines of such a flow, known as Hamel flow, is the basis of the gradual alignment of random CNTs into the fiber, which forms as a jet emanates from tip of the Taylor cone. The solution of the flow in axisymmetric polar coordinates $(r, \varepsilon, 0)$, as shown by figure 17, is given by

$$v_r = \frac{\nu F(\varepsilon)}{r}, \tag{13}$$

with

$$F(\varepsilon) = b\left\{3\tanh^2\left[\left(\sqrt{\frac{-b}{2}}\right)(\alpha - \varepsilon) + 1.146\right] - 2\right\}, \tag{14}$$

where v_r is the radial velocity, ν is the kinematic viscosity, α the wedge/cone half angle and b is a parameter that determines the inertial concentration of the flow into the cone vertex.

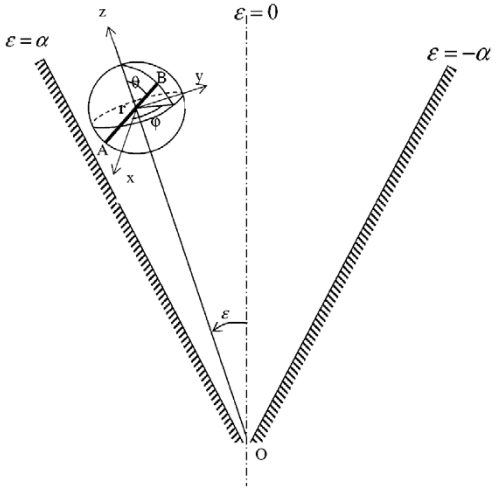

Figure 17. Schematic depiction of a wedge geometry of half angle α to represent the conical shape of an electrospinning meniscus indicating the polar coordinate system $(r, \varepsilon, 0)$ used to describe the bulk converging liquid flow towards the conical vertex and the axisymmetric spherical coordinate system (r, θ, ϕ) used to describe the rod-like particulate flow. Reproduced with permission from Y. Dror, W. Salalha, R.L. Khalfin, Y. Cohen, A.L. Yarin, E. Zussman, *Langmuir*, **19**, 7012 (2003). Copyright (2003), American Chemical Society.

The CNTs, on the other hand, are treated as rods in the flow which are sufficiently large such that random rotational motion can be neglected but small enough such that it translates along the streamlines at the local fluid velocity. The orientation of these rods can then be described by a probability distribution given by the Fokker–Planck equation with an additional term to account for orientation due to the flow. Adopting spherical coordinates (r, θ, ϕ) for the rods, the solution to the probability density function for the rod orientation W for rods aligned along the flow plane, i.e. $\phi = \pi/2$, then reads

$$W(\theta, t) = \frac{1}{4\pi \left| \sin\theta \left(\cos\theta + \frac{dF/d\varepsilon}{2F} \sin\theta \right) \right|^{3/2} \left| \frac{A}{(1+A^2)} \left(1 + \frac{dF/d\varepsilon}{2F} A \right) \right|^{3/2}}, \tag{15}$$

with

$$A = \frac{1}{2F \left[\frac{1}{\sin\theta} \left(\frac{\nu t}{r_o^2} + \frac{1}{2F} \right) \left(\cos\theta + \frac{dF}{d\varepsilon} \frac{\sin\theta}{2F} \right) - \frac{1}{4F^2} \frac{dF}{d\varepsilon} \right]}. \tag{16}$$

In the above, r_o is the initial rod position at time $t = 0$, which can be related to r by

$$\frac{r^2}{2\nu} = F(\varepsilon)t + \frac{r_o^2}{2\nu}. \tag{17}$$

The results for the streamline $\varepsilon = \alpha/10$ with $\alpha = \pi/6$ and $-b = 50$ are shown in figure 18 in which it can be seen that the particles tend to be aligned along the stream line.

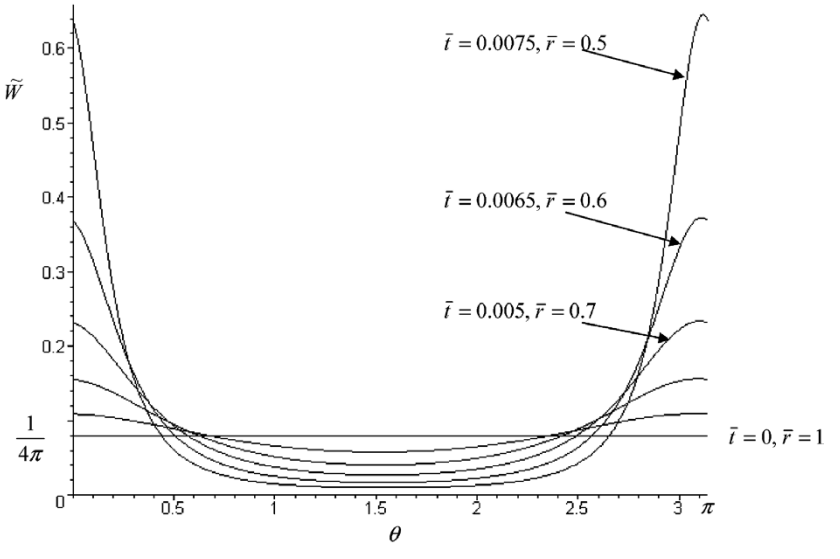

Figure 18. Particle probability density function along the streamline $\varepsilon = \alpha/10 = \pi/60$ with Reynolds number $(-b) = 50$. $\bar{r} = r/r_o$ is the dimensionless particle position and $\bar{t} = \nu t/r_o^2$ is the dimensionless time, and can be obtained from equation (17) with $\bar{r} = \sqrt{1 + 2F\bar{t}}$ with $F(\alpha/10) = -29$. Reproduced with permission from Y. Dror, W. Salalha, R.L. Khalfin, Y. Cohen, A.L. Yarin, E. Zussman, *Langmuir*, **19**, 7012 (2003). Copyright (2003), American Chemical Society.

The crucial assumption made in this analysis, however, should be noted, that is the presence of the CNTs in the flow do not modify the behaviour of the local flow itself, thus allowing the fluid and particle flows to be solved separately.

5. Future challenges

It can be seen that there is still a lack of thorough understanding in the electrospinning of composite nanofibers, and in particular theoretical or numerical studies to predict the behaviour of the CNTs within the electrospun nanofibers. The reason for this, granted the infancy of research in this area, is immediately recognisable given the difficulties involved in the electrohydrodynamic modelling of electrospinning on its own, as discussed above. The coupling between the fibers and the electrospinning flows adds an extra layer of complexity to the analysis. More experimentation to elucidate a fundamental understanding of these flows is also vital for advances in the field.

Further studies, both theoretical and experimental, are also required to understand how CNTs interact, both mechanically and chemically, with its surrounding polymer matrix, both at the micro/nanoscopic as well as the macroscopic scales, and hence how this translates into the enhanced composite nanofiber properties observed. This would allow the accurate prediction of how variation of the CNT system parameters e.g. SWNT/MWNT, concentration, dimensions, etc. affect the macroscopic mechanical, thermal and electrical properties. A large proportion of electrospun CNT embedded polymer fibers has been carried out using MWNTs. There is thus a need to investigate SWNT nanocomposite fibers in further detail. Part of the reason for the fewer studies of SWNT composite fibers compared to MWNT fibers is the difficulty in producing large amounts of SWNT. Nevertheless, the payoff is large since SWNTs hold promise of enhanced properties even beyond that of MWNTs. An in-depth discussion on the advantages and challenges of SWNT composite polymers can be found in Ajayan *et al.* [117]. Another crucial issue that needs resolving is how mechanical load is transferred from the polymer matrix to the CNTs, given that this is responsible for the enhancement of the critical fracture strain and the increased toughness reinforcement of the fiber.

There are processing and characterisation concerns that require resolution as well. For example, alternatives to sonification and other methods or conditions under which CNT damage is minimised during dispersion are required. Breuer and Sundararaj [29] suggest the assembly of CNTs into arrays or yarns as one possible method. Enhancing filler/matrix interfacial contact through stronger chemical bonding (surface reactivity) or increasing interfacial shear (surface roughness) to reduce slip by cross-linking CNTs is another, given its importance in determining the final composite nanofiber properties. Both chemical bonding strength and interfacial shear can be increased by surface functionalisation, chemical binding, surface coating or cross-linking individual CNTs or CNT arrays [118, 119]. Nevertheless, care must be taken when increasing interfacial shear, in particular if MWNTs are employed, to avoid shearing the concentric layers of the MWNTs [29].

As yet, it is also unclear whether dipole formation along the axis of CNTs can aid in its alignment along the fiber. It is without doubt the high dielectric polarisabilities

of CNTs [120, 121] give rise to strong dipole–dipole interactions in a dense solution of CNTs. In fact, given typical polarisabilities α along the CNT axis of order $10^2 L$ Å^2 [120], where $L \sim 1\,\mu$m is the characteristic nanotube axial length scale, the induced dipole attractive force, $\alpha E^2/2$, where E is the applied polarising field acting on the CNT which is approximately 10^7 V/m in electrospinning, is of the order 10^{-10} N. This is comparable to the hydrodynamic shear force, $2\pi RL(\mu U/L) \sim 10^{-10}$ N, where $R \sim 1$ nm is the CNT radius, $\mu \sim 10$ cp is the solution viscosity and $U \sim \gamma/\mu \sim 1$ m/s the characteristic velocity; $\gamma \sim 10$ dyne/cm is the surface tension. The above then suggests that dipole interaction due to the high applied fields play a role in aligning the CNTs along the fiber axis in addition to the hydrodynamic shear mechanism for CNT alignment proposed by Dror *et al*. [18]. Nevertheless, the high dielectric polarisabilities of CNT also give rise to field screening [120, 121] that results in an order of magnitude reduction in α [120] and consequently a weakening of the alignment effect [122].

Field screening, however, becomes negligible if high frequency AC fields are employed. In fact, Zhou *et al*. [123] have demonstrated that CNTs are aligned along the field lines of a planar T-electrode. Given that the CNTs are aligned along the field lines instead of the streamlines, the role of hydrodynamic alignment due to electroosmotic flow is eliminated. When low frequency AC fields were employed, however, no alignment was observed, therefore suggesting that field screening effects arise to reduce the CNT polarisability. The above therefore raises the possibility of enhanced CNT alignment within electrospun fibers using AC electrospraying techniques [47, 66], which is currently being explored by the authors.

We end on the note that although it has been shown that electrospinning is somewhat successful in aligning CNTs along the fiber axis, there is still much room for further systematic studies on improving alignment and reducing irregularities such as protrusion or convolution.

Acknowledgements

One of the authors (LYY) would like to express his gratitude to Dr Omar K. Matar at Imperial College London for helpful discussions on the electrospinning theory and to Professor Hsueh-Chia Chang at the University of Notre Dame for introducing him to the subject.

References

[1] S. Iijima. Helical microtubules of graphitic carbon. *Nature*, **354**, 56 (1991).
[2] Z.W. Pan, S.S. Xie, L. Lu, B.H. Chang, L.F. Sun, W.Y. Zhou, G. Wang, D.L. Zhang. Tensile tests of ropes of very long aligned multiwall carbon nanotubes. *Appl. Phys. Lett*., **74**, 3152 (1999).
[3] F. Li, H.M. Cheng, S. Bai, G. Su, M.S. Dresselhaus. Tensile strength of single-walled carbon nanotubes directly measured from their macroscopic ropes. *Appl. Phys. Lett*., **77**, 3161 (2000).
[4] S. Iijima, C. Brabec, A. Maiti, J. Bernholc. Structural flexibility of carbon nanotubes. *J. Chem. Phys*., **104**, 2089 (1996).
[5] O. Lourie, D.M. Cox, H.D. Wagner. Buckling and collapse of embedded carbon nanotubes. *Phys. Rev. Lett*., **81**, 1638 (1998).
[6] G.-M. Kim, G.H. Michler, P. Pötschke. Deformation processes of ultrahigh porous multiwalled carbon nanotubes/polycarbonate composite fibers prepared by electrospinning. *Polymer*, **46**, 7346 (2005).

[7] S.M. Bachilo, M.S. Strano, C. Kittrell, R.H. Hauge, R.E. Smalley, R.B. Weisman. Structure-assigned optical spectra of single-walled carbon nanotubes. *Science*, **298**, 2361 (2002).
[8] J. Hone, M.C. Llaguno, N.M. Nemes, A.T. Johnson. Electrical and thermal transport properties of magnetically aligned single wall carbon nanotube films. *Appl. Phys. Lett*., **77**, 666 (2000).
[9] M.S. Dresselhaus, G. Dresselhaus, P.C. Ecklund. *Science of Fullerenes and Carbon Nanotubes*, Academic, New York (1996).
[10] P.M. Ajayan. Nanotubes from carbon. *Chem. Rev*., **99**, 1787 (1999).
[11] R.H. Baughman, A.A. Zhakidov, W.A. de Heer. Carbon nanotubes – the route toward applications. *Science*, **297**, 787 (2002).
[12] T. Guo, P. Nikolaev, A.G. Rinzler, D. Tománek, D.T. Colbert, R.E. Smalley. Self-assembly of tubular fullerenes. *J. Phys. Chem*., **99**, 10694 (1995).
[13] G.G. Tibbetts. Carbon fibers produced by pyrolysis of natural gas in stainless steel tubes. *Appl. Phys. Lett*., **42**, 666 (1983).
[14] Z.F. Ren, Z.P. Huang, J.W. Xu, J.H. Wang, P. Bush, M.P. Siegal, P.N. Provencio. Synthesis of large arrays of well-aligned carbon nanotubes on glass. *Science*, **282**, 1105 (1998).
[15] S.B. Sinnott, R. Andrews. Carbon nanotubes: synthesis, properties and applications. *Crit. Rev. Solid State Mat. Sci*., **26**, 145 (2001).
[16] R. Tucknott, S.N. Yaliraki. Aggregation properties of carbon nanotubes at interfaces. *Chem. Phys*., **281**, 455 (2002).
[17] S. Lefrant, J.-P. Buisson, O. Chauvet, J.-M. Benoit, M. Baibarac, I. Baltog, P. Bernier. Interactions in carbon nanotubes and polymer/nanotubes composites as evidenced by Raman spectroscopy. *Mater. Res. Soc. Proc*., Vol. 746, Paper Z7.2 (2001).
[18] Y. Dror, W. Salalha, R.L. Khalfin, Y. Cohen, A.L. Yarin, E. Zussman. Carbon nanotubes embedded in oriented polymer nanofibers by electrospinning. *Langmuir*, **19**, 7012 (2003).
[19] M.J. Biercuk, M.C. Llaguno, M. Radosavljevic, J.K. Hyun, A.T. Johnson. Carbon nanotube composites for thermal management. *Appl. Phys. Lett*., **80**, 2767 (2002).
[20] Y.A. Kim, T. Hayashi, Y. Fukai, M. Endo, T. Yanagisawa, M.S. Dresselhaus. Effect of ball milling on morphology of cup-stacked carbon nanotubes. *Chem. Phys. Lett*., **355**, 279 (2002).
[21] B. Vigolo, A. Pénicaud, C. Coulon, C. Sauder, R. Pailler, C. Journet, P. Bernier, P. Poulin. Macroscopic fibers and ribbons of oriented carbon nanotubes. *Science*, **290**, 1331 (2000).
[22] B.W. Smith, Z. Benes, D.E. Luzzi, J.E. Fischer, D.A. Walters, M.J. Casavant, J. Schmidt, R.E. Smalley. Structural anisotropy of magnetically aligned single wall carbon nanotube films. *Appl. Phys. Lett*., **77**, 663 (2000).
[23] S. Kumar, H. Doshi, M. Srinivasarao, J.O. Park, D.A. Schiraldi. Fibers from polypropylene/nano carbon fiber composites. *Polymer*, **43**, 1701 (2002).
[24] L. Jin, C. Bower, O. Zhou. Alignment of carbon nanotubes in a polymer matrix by mechanical stretching. *Appl. Phys. Lett*., **73**, 1997 (1998).
[25] C. Bower, R. Rosen, L. Jin, J. Han, O. Zhou. Deformation of carbon nanotubes in nanotube-polymer composites. *Appl. Phys. Lett*., **74**, 3317 (1999).
[26] B.Z. Tang, H. Xu. Preparation, alignment, and optical properties of soluble poly(phenylacetylene)-wrapped carbon nanotubes. *Macromolecules*, **32**, 2569 (1999).
[27] E.K. Hobbie, H. Wang, H. Kim, S. Lin-Gibson, E.A. Grulke. Orientation of carbon nanotubes in a sheared polymer melt. *Phys. Fluids*, **15**, 1196 (2003).
[28] R.R. Schlittler, J.W. Seo, J.K. Gimzewski, C. Durkan, M.S.M. Saifullah, M.E. Welland. Single crystals of single-walled carbon nanotubes formed by self-assembly. *Science*, **292**, 1136 (2001).
[29] O. Breuer, U. Sundararaj. Big returns from small fibers: a review of polymer/carbon nanotube composites. *Polym. Comp*., **25**, 630 (2004).
[30] R. Dersch, M. Steinhart, U. Boudriot, A. Greiner, J.H. Wendorff. Nanoprocessing of polymers: applications in medicine, sensors, catalysis, photonics. *Polym. Adv. Technol*., **16**, 276 (2005).
[31] S.A. Curran, P.A. Ajayan, W.J. Blau, D.L. Carroll, J.N. Coleman, A.B. Dalton, A.P. Davey, A. Drury, B. McCarthy, S. Maier, A. Strevens. A composite from poly(m-phenylenevinylene-co-2,5-dioctoxy-p-phenylenevinylene) and carbon nanotubes: a novel material for molecular optoelectronics. *Adv. Mater*., **10**, 1091 (1998).
[32] I.D. Norris, M.M. Shaker, F.K. Ko, A.G. MacDiarmid. Electrostatic fabrication of ultrafine conducting fibers: polyaniline/polyethylene oxide blends. *Synth. Met*., **114**, 109 (2000).
[33] K. Bradley, J.-C.P. Gabriel, G. Grüner. Flexible nanotube electronics. *Nano Lett*., **3**, 1353 (2003).
[34] E. Kymakis, G.A.J. Amaratunga. Optical properties of polymer-nanotube composites. *Synth. Met*., **142**, 161 (2004).
[35] P.P. Tsai, H. Schreuder-Gibson, P. Gibson. Different electrostatic methods for making electret filters. *J. Electrostatics*, **54**, 333 (2002).
[36] P.W. Gibson, H.L. Schreuder-Gibson, C. Pentheny. Electrospinning technology: direct application of tailorable ultrathin membranes. *J. Coated Fabrics*, **28**, 63 (1998).

[37] P. Gibson, H. Schreuder-Gibson, D. Rivin. Transport properties of porous membranes based on electrospun nanofibers. *Colloid Surf. A: Phys. Eng. Aspects*, **187–188**, 469 (2001).
[38] C. Park, Z. Ounaies, K.A. Watson, K. Pawlowski, S.E. Lowther, J.W. Connell, E. Siochi, J.S. Harrison, T.L. St. Clair. Polymer-single wall carbon nanotube composites for potential spacecraft applications. *NASA Center for AeroSpace Information ICASE Report No. 2002-36*, *NASA/CR-2002-211940* (2002).
[39] J.G. Smith Jr, J.W. Connell, D.M. Delozier, P.T. Lillehei, K.A. Watson, Y. Lin, B. Zhou, Y.-P. Sun. Space durable polymer/carbon nanotube films for electrostatic charge mitigation. *Polymer*, **45**, 825 (2004).
[40] M. Steinhart, S. Senz, R.B. Wehrspohn, U. Gösele, J.H. Wendorff. Curvature-directed crystallization of poly(vinylidene difluoride) in nanotube walls. *Macromolecules*, **36**, 3646 (2003).
[41] M. Tahhan, V.-T. Truong, G.M. Spinks, G.G. Wallace. Carbon nanotube and polyaniline composite actuators. *Smart Mater. Struc.*, **12**, 626 (2003).
[42] Z.-M. Huang, Y.-Z. Zhang, M. Kotaki, S. Ramakrishna. A review on polymer nanofibers by electrospinning and their applications in nanocomposites. *Comp. Sci. Tech.*, **63**, 2223 (2003).
[43] M. Chasin, R. Langer (Eds) *Biodegradable Polymers as Drug Delivery Systems*, Marcel Dekker, New York (1990).
[44] X. Zong, K. Kim, D. Fang, S. Ran, B.S. Hsiao, B. Chu. Structure and process relationship of electrospun bioabsorbable nanofiber membranes. *Polymer*, **43**, 4403 (2002).
[45] G. Wnek, M.E. Carr, D.G. Simpson, G.L. Bowlin. Electrospinning of nanofiber fibrinogen structures. *Nano Lett.*, **3**, 213 (2003).
[46] P.P. Joshi, S.A. Merchant, Y. Wang, D.W. Schmidtke. Amperometric biosensors based on redox polymer–carbon nanotube–enzyme composites. *Anal. Chem.*, **77**, 3183 (2005).
[47] L.Y. Yeo, Z. Gagnon, H.-C. Chang. AC Electrospray biomaterials synthesis. *Biomaterials*, **26**, 6122 (2005).
[48] R. Haggenmueller, H.H. Gommans, A.G. Rinzler, J.E. Fischer, K.E. Winey. Aligned single-wall carbon nanotubes in composites by melt processing methods. *Chem. Phys. Lett.*, **330**, 219 (2000).
[49] B. Safadi, R. Andrews, E.A. Grulke. Multiwalled carbon nanotube polymer composites: synthesis and characterization of thin films. *J. Appl. Polym. Sci.*, **84**, 2660 (2002).
[50] Z. Jia, Z. Wang, C. Xu, J. Liang, B. Wei, D. Wu, S. Zhu. Study on poly(methyl methacrylate)/carbon nanotube composites. *Mater. Sci. Eng. A*, **271**, 395 (1999).
[51] R. Andrews, D. Jacques, M. Minot, T. Rantell. Fabrication of carbon multiwall nanotube/polymer composites by shear mixing. *Macromol. Mater. Eng.*, **287**, 395 (2002).
[52] P.K. Wu, J. Fitz-Gerald, A. Pique, D.B. Chrisey, R.A. McGill. Deposition of nanotubes and nanotube composites using matrix-assisted pulsed laser evaporation. *Mater. Res. Soc. Proc.*, Vol. 617, Paper J2.3 (2000).
[53] E.T. Thostenson, W.Z. Li, D.Z. Wang, Z.F. Ren, T.W. Chou. Carbon nanotube/carbon fiber hybrid multiscale composites. *J. Appl. Phys.*, **91**, 6034 (2002).
[54] J. Zeleny. The electrical discharge from liquid points, and a hydrostatic method of measuring the electric intensity at their surfaces. *Phys. Rev.*, **3**, 69 (1914).
[55] J.B. Fenn, M. Mann, C.K. Meng, S.F. Wong, C.M. Whitehouse. Electrospray ionization for mass spectrometry of large biomolecules. *Science*, **246**, 64 (1989).
[56] P.K. Baumgarten. Electrostatic spinning of acrylic microfibers. *J. Colloid Interface Sci.*, **36**, 71 (1971).
[57] A. Fromhals., Process and apparatus for preparing artificial threads. US Patent No. 1,975,504 (1934).
[58] E.K. Gladding. Apparatus for the production of filaments, threads and the like. US Patent No. 2,168,027 (1939).
[59] L. Larrondo, R. St. John Manley. Electrostatic fiber spinning from polymer melts. I. Experimental observations on fiber formation and properties. *J. Polym. Sci. B: Polym. Phys.*, **19**, 909 (1981).
[60] J. Doshi, D.H. Reneker. Electrospinning process and applications of electrospun fibers. *J. Electrostatics*, **35**, 151 (1995).
[61] J.-S. Kim, D.H. Reneker. Polybenzimidazole nanofiber produced by electrospinning. *Polym. Eng. Sci.*, **39**, 849 (1999).
[62] J.-S. Kim, D.S. Lee. Thermal properties of electrospun polyesters. *Polymer J.*, **32**, 616 (2000).
[63] C.J. Buchko, L.C. Chen, Y. Shen, D.C. Martin. Processing and microstructural characterization of porous biocompatible protein polymer thin films. *Biomaterials*, **40**, 7397 (1999).
[64] J.A. Matthews, G.E. Wnek, D.G. Simpson, G.L. Bowlin. Electrospinning of collagen nanofibers. *Biomacromolecules*, **3**, 232 (2002).
[65] E.-R. Kenawy, J.M. Layman, J.R. Watkins, G.L. Bowlin, J.A. Matthews, D.G. Simpson, G.E. Wnek. Electrospinning of poly(ethylene-co-vinyl alcohol) fibers. *Biomaterials*, **24**, 907 (2003).
[66] L.Y. Yeo, D. Lastochkin, S.-C. Wang, H.-C. Chang. A new AC electrospray mechanism by Maxwell-Wagner polarization and capillary resonance. *Phys. Rev. Lett.*, **92**, 133902 (2004).
[67] D.H. Reneker, A.L. Yarin, H. Fong, S. Koombhongse. Bending instability of electrically charged liquid jets of polymer solutions in electrospinning. *J. Appl. Phys.*, **87**, 4531 (2000).

[68] Y. Dzenis. Spinning continuous fibers for nanotechnology. *Science*, **304**, 1917 (2004).
[69] J.M. Deitzel, J. Kleinmeyer, J.K. Hirvonen, N.C. Beck Tan. Controlled deposition of electrospun poly(ethylene oxide) fibers. *Polymer*, **42**, 8163 (2001).
[70] J. Kameoka, H.G. Craighead. Fabrication of oriented polymeric nanofibers on planar surfaces by electrospinning. *Appl. Phys. Lett.*, **83**, 371 (2003).
[71] A. Theron, E. Zussman, A.L. Yarin. Electrostatic field-assisted alignment of electrospun nanofibers. *Nanotechnology*, **12**, 384 (2001).
[72] M. Clopeau, B. Prunet-Foch. Electrostatic spraying of liduids: main functioning modes. *J. Electrostat.*, **25**, 165 (1990).
[73] M. Clopeau, B. Prunet-Foch. Electrohydrodynamical spraying functioning modes: a critical review. *J. Aerosol Sci.*, **25**, 1021 (1994).
[74] J.M. Grace, J.C.M. Marijnissen. A review of liquid atomization by electrical means. *J. Aerosol Sci.*, **25**, 1005 (1994).
[75] J.M. Deitzel, J. Kleinmeyer, D. Harris, N.C. Beck Tan. The effect of processing variables on the morphology of electrospun nanofibers and textiles. *Polymer*, **42**, 261 (2001).
[76] H.-C. Chang, E.A. Demekhin, E. Kalaidin. Iterated stretching of viscoelastic jets. *Phys. Fluids*, **11**, 1717 (1999).
[77] A.L. Yarin, E. Zussman. Upward needleless electrospinning of multiple nanofibers. *Polymer*, **45**, 2977 (2004).
[78] Y. Zhou, M. Freitag, J. Hone, C. Staii, A.T. Johnson Jr, N.J. Pinto, A.G. MacDiarmid. Fabrication and electrical characterization of polyaniline-based nanofibers with diameter below 30 nm. *Appl. Phys. Lett.*, **83**, 3800 (2003).
[79] H. Fong, D.H. Reneker. Elastometric nanofibers of styrene-butadiene-styrene triblock copolymer. *J. Polym. Sci. B: Polym. Phys.*, **37**, 3488 (1999).
[80] M.M. Demir, I. Yilgor, E. Yilgor, B. Erman. Electrospinning of polyurethane fibers. *Polymer*, **43**, 3303 (2002).
[81] H. Fong, D.H. Reneker, Electrospinning and the formation of nanofibers. In *Structure Formation in Polymeric Fibers*, D.R. Salem (Ed.), pp. 225–246, Hanser, Munich (2001).
[82] D.-R. Chen, D.Y.H. Pui, S.L. Kaufman. Electrospraying of conducting liquids for monodispersed aerosol generation in the 4 nm to 1.8 μm range. *J. Aerosol Sci.*, **26**, 963 (1995).
[83] M. Bognitzki, W. Czado, T. Frese, A. Schaper, M. Hellwig, M. Steinhart, A. Greiner, J.H. Wendorff. Nanostructured fibers via electrospinning. *Adv. Mater.*, **13**, 70 (2001).
[84] W.-J. Li, C.T. Laurencin, E.J. Caterson, R.S. Tuan, F.K. Ko. Electrospun nanofibrous structure: a novel scaffold for tissue engineering. *J. Biomed. Mater. Res.*, **60**, 613 (2002).
[85] I.G. Loscertales, A. Barrero, I. Guerrero, R. Cortijo, M. Marquez, A.M. Gañán-Calvo. Micro/Nano encapsulation via electrified co-axial liquid jets. *Science*, **295**, 1695 (2002).
[86] Z. Sun, E. Zussman, A.L. Yarin, J.H. Wendorff, A. Greiner. Compound core-shell polymer nanofibers by co-electrospinning. *Adv. Mater.*, **15**, 1929 (2003).
[87] D. Li, Y. Xia. Direct fabrication of composite and ceramic hollow nanofibers by electrospinning. *Nano Lett.*, **4**, 933 (2004).
[88] F. Ko, Y. Gogotsi, A. Ali, N. Naguib, H. Ye, G. Yang, C. Li, P. Willis. Electrospinning of continuous carbon nanotube-filled nanofiber yarns. *Adv. Mater.*, **15**, 1161 (2003).
[89] C. Seoul, Y.-T. Kim, C.-K. Baek. Electrospinning of poly(vinylidene fluoride)/dimethylformamide solutions with carbon nanotubes. *J. Polym. Sci. B: Polym. Phys.*, **41**, 1572 (2003).
[90] H. Ye, H. Lam, N. Titchenal, Y. Gogotsi, F. Ko. Reinforcement and rupture behavior of carbon nanotubes–polymer nanofibers. *Appl. Phys. Lett.*, **85**, 1775 (2004).
[91] J.J. Ge, H. Hou, Q. Li, M.J. Graham, A. Greiner, D.H. Reneker, F.W. Harris, S.Z.D. Cheng. Assembly of well-aligned multiwalled carbon nanotubes in confined polyacrylonitrile environments: electrospun composite nanofiber sheets. *J. Am. Chem. Soc.*, **126**, 15754 (2004).
[92] S. Banda. Characterization of aligned carbon nanotube/polymer composites. MS thesis, Virginia Commonwealth University (2004).
[93] J. Liu, T. Wang, T. Uchida, S. Kumar. Carbon nanotube core–polymer shell nanofibers. *J. Appl. Polym. Sci.*, **96**, 1992 (2005).
[94] J.C. Kearns, R.L. Shambaugh. Polypropylene fibers reinforced with carbon nanotubes. *J. Appl. Polym. Sci.*, **86**, 2079 (2002).
[95] K. Yamamoto, S. Akita, Y. Nakayama. Orientation and purification of carbon nanotubes using ac electrophoresis. *J. Phys. D: Appl. Phys.*, **31**, L34 (1998).
[96] M.J. O'Connell, P. Boul, L.M. Ericson, C. Huffman, Y. Wang, E. Haroz, C. Kuper, J. Tour, K.D. Ausman, R.E. Smalley. Reversible water-solubilization of single-walled nanotubes by polymer wrapping. *Chem. Phys. Lett.*, **342**, 265 (2001).

[97] C. Velasco-Santos, A.L. Martínez-Hernández, M. Lozada-Cassou, A. Alvarez-Castillo, V.M. Castaño. Chemical functionalization of carbon nanotubes through an organosilane. *Nanotechnology*, **13**, 495 (2002).
[98] T. Prasse, A. Ivankov, J. Sandler, K. Schulte, W. Bauhofer. Imaging of conductive filler networks in heterogeneous materials by scanning Kelvin microscopy. *J. Appl. Polym. Sci.*, **82**, 3381 (2001).
[99] D. Qian, E.C. Dickey, R. Andrews, T. Rantell. Load transfer and deformation mechanisms in carbon nanotube-polystyrene composites. *Appl. Phys. Lett.*, **76**, 2868 (2000).
[100] G.I. Taylor. Disintegration of water drops in an electric field. *Proc. Roy. Soc. Lond. A*, **280**, 383 (1964).
[101] H. Li, T.C. Halsey, A. Lobkovsky. Singular shape of a fluid drop in an electric or magnetic field. *Europhys. Lett.*, **27**, 575 (1994).
[102] A. Ramos, A. Castellanos. Conical points in liquid-liquid interfaces subjected to electric fields. *Phys. Lett. A*, **184**, 268 (1994).
[103] M.M. Hohman, M. Shin, G. Rutledge, M.P. Brenner. Electrospinning and electrically forced jets. I. Stability theory. *Phys. Fluids*, **13**, 2201 (2001).
[104] D.A. Saville. Electrohydrodynamics: the Taylor-Melcher leaky dielectric model. *Annu. Rev. Fluid Mech.*, **29**, 27 (1997).
[105] E.J. Hinch. *Perturbation Methods*, Cambridge University, Cambridge (1991).
[106] S. Maheshwari, L.Y. Yeo, H.-C. Chang. High frequency AC electrosprays. Submitted to *Phys. Fluids*.
[107] V.N. Kirichenko, I.V. Petryanov-Sokolov, N.N. Suprun, A.A. Shutov. Asymptotic radius of a slightly conducting liquid jet in an electric field. *Sov. Phys. Dokl.*, **31**, 611 (1986).
[108] J.J. Feng. The stretching of an electrified non-Newtonian jet: a model for electrospinning. *Phys. Fluids*, **14**, 3912 (2002).
[109] M.M. Hohman, M. Shin, G. Rutledge, M.P. Brenner. Electrospinning and electrically forced jets. II. Applications. *Phys. Fluids*, **13**, 2221 (2001b).
[110] A.M. Gañán-Calvo. On the theory of electrohydrodynamically driven capillary jets. *J. Fluid Mech.*, **335**, 165 (1997).
[111] R.P.A. Hartman, D.J. Brunner, D.M.A. Camelot, J.C.M. Marijnissen, B. Scarlett. Electrohydrodynamic atomization in the cone-jet mode physical modeling of the liquid cone and jet. *J. Aerosol Sci.*, **30**, 823 (1999).
[112] W.N. Song, Z.M. Xia. A phenomenological viscosity model for polymeric fluid. *J. Non-Newtonian Fluid Mech.*, **53**, 151 (1994).
[113] A.F. Spivak, Y.A. Dzenis, D.H. Reneker. A model of steady state jet in the electrospinning process. *Mech. Res. Comm.*, **27**, 37 (2000).
[114] J. Jeans. *The Mathematical Theory of Electricity and Magnetism*, Cambridge University, Cambridge (1925).
[115] A.L. Yarin, S. Koombhongse, D.H. Reneker. Bending instability in electrospinning of nanofibers. *J. Appl. Phys.*, **89**, 3018 (2001).
[116] S. Grigoras, A.A. Gusev, S. Santos, U.W. Suter. Evaluation of the elastic constants of nanoparticles from atomistic simulations. *Polymer*, **43**, 489 (2002).
[117] P.M. Ajayan, L.S. Schadler, C. Giannaris, A. Rubio. Single-walled carbon nanotube–polymer composites: strength and weakness. *Adv. Mater.*, **12**, 750 (2000).
[118] J.-P. Salvetat, J.-M. Bonard, N.H. Thomson, A.J. Kulik, L. Forró, W. Benoit, L. Zuppiroli. Mechanical properties of carbon nanotubes. *Appl. Phys. A*, **69**, 255 (1999).
[119] J.H. Chen, Z.P. Huang, D.Z. Wang, S.X. Yang, J.G. Wen, Z.F. Ren. Electrochemical synthesis of polypyrrole/carbon nanotube nanoscale composites using well-aligned carbon nanotube arrays. *Appl. Phys. A*, **73**, 129 (2001).
[120] L.X. Benedict, S.G. Louie, M.L. Cohen. Static polarizabilities of single-wall carbon nanotubes. *Phys. Rev. B*, **52**, 8541 (1995).
[121] L. Lou, P. Nordlander, R.E. Smalley. Fullerene nanotubes in electric fields. *Phys. Rev. B*, **52**, 1429 (1995).
[122] M.J. Casavant, D.A. Walters, J.J. Schmidt, R.E. Smalley. Neat macroscopic membranes of aligned carbon nanotubes. *J. Appl. Phys.*, **93**, 2153 (2003).
[123] R. Zhou, P. Wang, H.-C. Chang. Bacteria capture, concentration and detection based on AC dielectrophoresis and self-assembly of polarizable single-wall carbon nanotubes. *Electrophoresis*, **27,** 1376 (2006).